

Mitigation of Solid Booster Ignition over Pressure by Water Aerosol Sprays

Viatcheslav Osipov,* Michael Khasin,† and Halyna Hafiychuk‡

Stinger Ghaffarian Technologies, Inc., NASA Ames Research Center, Moffett Field, California 94035

Cyrill Muratov‡

New Jersey Institute of Technology, Newark, New Jersey 07102

Michael Watson‡

NASA Marshall Space Flight Center, Huntsville, Alabama 35812

and

Vadim Smelyanskiy§

NASA Ames Research Center, Moffett Field, California 94035

DOI: 10.2514/1.A33110

Interaction of acoustic waves with water aerosol layers is analyzed in the context of the problem of solid booster ignition overpressure suppression. In contrast to the conventional approach to ignition overpressure suppression, which aims at using water to quench the sources of the ignition overpressure waves, this study focuses on blocking the ignition overpressure wave propagation, using reflection and attenuation of the wave by the water aerosol layers. The study considers interaction of the waves with aerosol layers of large mass loading for varying sizes of the droplets. The size of the droplets is shown to substantially affect the mechanisms of interaction with the waves. The criteria for the crossover between different mechanisms are established as functions of the droplet size and the ignition overpressure wave parameters. The optimal parameters and designs for water aerosol sprays are proposed that maximize the ignition overpressure suppression. These results were obtained using the nozzle and the exhaust hole geometries similar to those of the space shuttle. Remarkably, it is found that various a priori reasonable designs of the aerosol and water sprays may increase the ignition overpressure impact on the vehicle, increasing the risk of vehicle damage.

Nomenclature

C_D	=	drag coefficient
C_P	=	specific heat at constant pressure, J/kg/K
c	=	sound velocity, m/s
d_{drop}	=	droplet diameter, m
f_L	=	liquid volume fraction
h	=	layer width, m
j	=	mass flux, kg/m ² /s
k	=	wave vector, 1/m
L_D	=	thermodiffusion length, m
M	=	million
p	=	fluid pressure, Pa
R_g	=	gas constant, J/kg/K
r_{drop}	=	droplet radius, m
T	=	fluid temperature, K
T_{aer}	=	transmission coefficient
T_{wave}	=	period of acoustic wave, s
t	=	time, s
u	=	gas velocity, m/s
α	=	attenuation coefficient, m ⁻¹
κ	=	thermal conductivity, W/m/K
λ	=	wavelength, m

μ	=	dynamic viscosity, Pa · s
ν	=	frequency, Hz
ρ	=	fluid mass density, kg/m ³
σ	=	surface tension, N/m
σ_{st}	=	Stefan–Boltzmann constant
τ	=	typical time, s
ω	=	angular frequency

Subscripts

aer	=	aerosol
drop	=	droplet
G	=	gas
ign	=	ignition
L	=	liquid
s	=	surface, saturation
v	=	vapor
w	=	water
0	=	initial state

I. Introduction

THE time window of ignition and postignition transient of solid rocket boosters (SRBs) is a dangerous moment during the launch of heavy lift rockets. This transient is characterized by the generation of a strong ignition overpressure (IOP) wave in the exhaust hole [1–8]. The IOP wave may propagate toward the vehicle and potentially inflict vehicle damage or result in the vehicle's shifting from the nominal position. During its first flight (April 1981), the STS-1 Space Shuttle was exposed to a strong IOP [1].

To mitigate the IOP effects that were discovered during the STS-1 mission, numerous experimental, analytical, and numerical studies were carried out [2,7–17]. The authors of [7,8] performed three-dimensional computational fluid dynamics (CFD) studies of the postignition acoustic waves in the launch environment. Scaling of the IOP applied to the space shuttle model was studied in [9,10]. The authors of [11] studied the effect of adding water to the SRB exhaust

Received 10 July 2014; revision received 18 November 2014; accepted for publication 20 November 2014; published online 10 February 2015. Copyright © 2014 by the American Institute of Aeronautics and Astronautics, Inc. The U.S. Government has a royalty-free license to exercise all rights under the copyright claimed herein for Governmental purposes. All other rights are reserved by the copyright owner. Copies of this paper may be made for personal or internal use, on condition that the copier pay the \$10.00 per-copy fee to the Copyright Clearance Center, Inc., 222 Rosewood Drive, Danvers, MA 01923; include the code 1533-6794/15 and \$10.00 in correspondence with the CCC.

*Senior Research Scientist, Applied Physics Group.

†Research Scientist, Applied Physics Group.

‡Professor, Department of Mathematical Sciences.

§System Engineering, Chief Engineer Office EE11.

¶Principal Scientist, Applied Physics Group.

plume and found that it significantly reduced the impact of IOP on the vehicle. Water sprays were also used to reduce heating of the platform and the deflector [1]. The latter effect was studied numerically in recent work [12]. A water spray system and water-filled bags at the mouth of the exhaust hole were used in STS-2 and in all the subsequent missions in order to control IOP [1]. The effect of the water bags was analyzed in [13].

A common approach to water suppression is to consider its effects on quenching of the gas thermal energy (plume cooling) due to evaporation of the liquid and vapor heating. Cooling the plume increases the density and reduces the volume of the exhaust gas leading to decrease in overpressure [15,16]. However, despite the apparent success of the water suppression system in the space shuttle missions, quantitative understanding of the exhaust gas quenching and the degree of liquid–gas mixing in real plumes is unknown. The two-phase dynamics of interacting exhaust gas and water sprays is very complex and not fully understood [15], and quantitative predictions for the IOP suppression are very difficult to establish. Consequently, the optimization of the IOP suppression design for modern vehicles, such as the Space Launch System, is still an empirical endeavor and is likely to face challenges, in particular at the point of extrapolating the experimental data on water suppression in the subscale vehicle tests to the full-scale rockets.

The present work focuses on an alternative approach to the IOP water suppression, aiming at suppression of the IOP wave itself rather than its source. The suppression is proposed to be achieved by optimized water aerosol sprays injected into or above the exhaust holes. Note that the effectiveness of aerosol sprays to mitigate blast waves was established by numerous studies in the context of military applications [18]. The main effects of the aerosol–IOP wave interaction are reflection and absorption of the wave by the aerosol, creating a barrier to prevent the wave from propagating into the space above the launch platform. In this respect, the effect of the aerosol is similar to the effect of water bags used in the space shuttle launches. The advantage of using aerosols instead of water bags, however, is that the weight of aerosols does not need to be supported by the launch platform. Thus, aerosols could be injected into the exhaust holes with complicated geometries, such as that of the Space Launch System. Furthermore, the optimization of a water suppression system design may be achieved by varying the parameters of the aerosols, such as the water droplet size, the water mass fraction and the droplet velocity in the sprays, and the design of the water nozzles in the exhaust holes.

The interaction of water aerosols with the exhaust plume was studied by Canabal and Frendi, who developed a high-fidelity computational model [17]. They analyzed various configurations of aerosol sprays and found that the majority of the configurations led to an increase in the IOP. They also found some configurations leading to IOP suppression. However, the relations between the aerosol and the wave properties, the exhaust hole geometry, and the IOP wave suppression efficiency were not analyzed previously. These relations are explored in the present work. In particular, the dependencies of the transmission and reflection coefficients of the acoustic waves in aerosols on the droplet diameter, the spectral characteristics of the IOP wave, and the geometries of the exhaust hole and the nozzle are studied. The analysis is performed both analytically and numerically. The ANSYS CFD software was used to carry out the numerical simulations.

The outline of the paper is as follows. In Sec. II, the characteristic values of the relevant IOP wave parameters are given. Section III explores the main physical processes determining the transmission and reflection of IOP pulses in the considered aerosol layers. There, estimates of the aerosols parameters (droplet size, average density, layer width) maximizing IOP suppression are made. Scaling predictions are also given, which may guide the design and interpretation of the subscale water suppression tests. Numerical details of the CFD simulations are presented in Sec. IV. Section V presents the results of the IOP suppression simulations in the established optimal parametric regime in a launch vehicle environment with axisymmetric geometry. There, it is shown that the aerosol layers with certain droplet sizes may efficiently reflect the IOP wave in the full-scale

rocket, whereas they reflect the IOP wave only weakly in a subscale model. It is proposed that a very efficient IOP suppression system may be built, using an optimized design of the aerosol sprays to replace the water bags. Section VI is the concluding section.

II. IOP Parameters

In this section, the typical values of the IOP parameters for the SRB used by the space shuttle are given, with the purpose of using them as a reference for the analysis of interaction of the acoustic wave with aerosol layers in the subsequent sections.

The duration of the IOP transient is about 0.5 s, and the typical overpressure time trace near the nozzle is a set of pulses with magnitudes up to 0.25 atm [1]. The results of the ANSYS simulations for an axisymmetric geometry with the parameters close to those of the space shuttle SRB and to its 5% subscale version are shown in Fig. 1 (see Sec. IV for the description of the numerical methods).

The schematics of the water nozzle location and the IOP wave propagation direction are shown in Fig. 1b. The ascending wave may be either the wave originating below the water sprays and transmitted through the aerosol layer or the wave originating above the sprays and reflected from the aerosol layer upward. The dynamics of the pressure transient is very complex. The most dangerous early stage of the IOP is characterized by a number of pressure spikes (Fig. 1). The first spike is associated with the overpressure wave originating at the nozzle.

The supersonic (with respect to the ambient gas) motion of the hot gas in the plume initiated by the sharp growth of temperature in the combustion chamber creates an overpressure wave (“first wave”) propagating out of the plume from the nozzle exit in the downstream direction. Passing through the nozzle exit, the first wave diffracts on the nozzle lip, leading to a relatively weak wave propagating toward the vehicle and determining the maximum pressure in the first spike. More important, the main component of the first wave keeps on propagating in the downstream direction. The second spike is associated with the ascending wave (“second wave”) created by an open-end reflection of the descending first wave from the bottom opening of the exhaust hole. The third spike is associated with the ascending wave (“third wave”) originating near the deflector downstream of the exhaust hole. The characteristic values of the IOP parameters (gas velocity, temperature, and pressure) for an axisymmetric geometry corresponding to the third wave are summarized in Fig. 2. One can see that the typical gas temperature outside the plume is close to 300 K, whereas the gas velocity approaches 70 m/s in the exhaust hole outside the plume. Inside the plume near its boundary, the gas temperature and velocity are close to 1300 K and 1500 m/s, respectively. According to Fig. 1, the approximate amplitude of the main IOP peaks near the nozzle exit and the skirt is $\Delta p = \pm 0.25$ atm. Their typical durations and the corresponding wavelengths are, respectively, $\tau_{\text{pulse}} \approx 30$ ms and $l_g \approx c_g \tau_{\text{pulse}} \approx 10$ m for the base geometry, and $\tau_{\text{pulse}} \approx 1.5$ ms and $l_g \approx 0.5$ m for the 5% subscale model. These parameters will be used in the subsequent estimates and numerical simulations.

III. Interaction of Overpressure Waves with Aerosol Layers

In their full generality, the physical processes involved in the reflection and transmission of acoustic waves in a dense aerosol of water droplets in the air are very complicated. Their theoretical studies have a long history [19–22]. To date, two limiting cases have been investigated. The first case is that of sound propagation in aerosols for sufficiently small Reynolds numbers. Here, the drag exerted by the gas on the droplets is governed by the Stokes law. In this linear drag regime, the transmission and the reflection coefficients have been calculated for finite attenuation [22]. The second case is that of strong waves, when the drag becomes nonlinear and eventually turbulent. In the nonlinear regime, the limit of small mass loading of the aerosol has been discussed in [23,24]. The parametric regime of interest in the present work does not fall within either one of

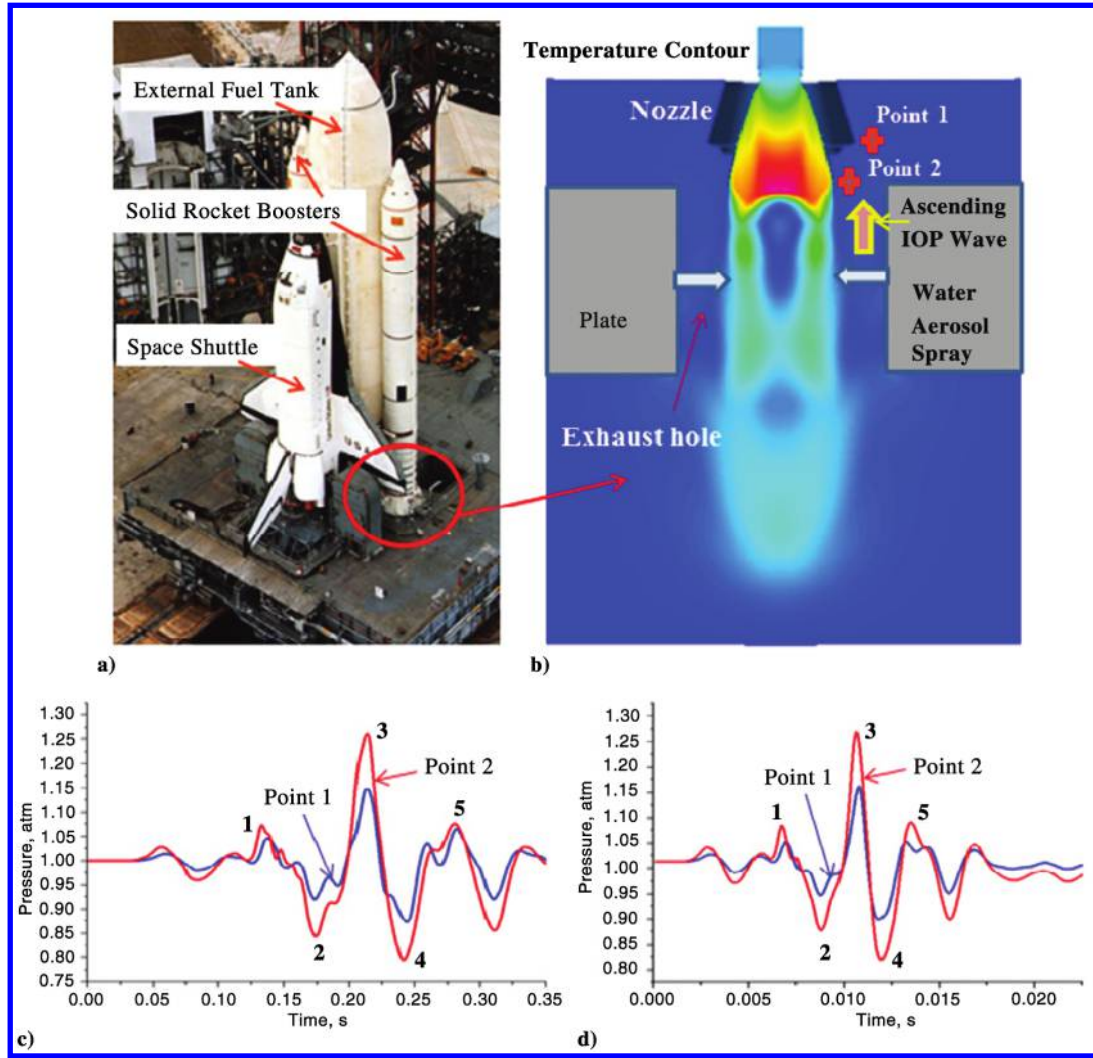


Fig. 1 The space shuttle (a), computational model (b), pressure at points 1 and 2, full scale (c), and 5% scale (d).

the two limits. The limit of the small mass loading is not relevant in the water suppression context. The regime of the Stokes law also does not apply to the IOP waves (Sec. III.A).

In the present work, several controlled approximations are made that simplify the complex picture of IOP–aerosol interaction and give an idea of the orders of magnitude of the relevant effects. These estimates are further used to guide a more refined computational analysis, using ANSYS software and various droplet–fluid interaction models built into its code. It will be assumed that the volume fraction of water is small, $f_L \ll 1$, whereas the mass loading (the density of the water–air mixture) is large. One may distinguish two extremes: the case of small droplets (fine aerosol or mist) and the case of large droplets (coarse aerosol).

The distinction is based on whether or not the droplets are entrained sufficiently fast by the gas movement in the wave on the timescale of the IOP pulse duration. The fast entrainment of the small droplets allows us to consider the mist as a homogenous medium with aerosol density for the propagation of an incoming IOP wave. In this case, the intensity of the transmitted wave, and therefore the efficiency of IOP wave suppression, is determined by the reflection of the incident wave from the aerosol layer. In the opposite case of coarse aerosol, the large droplets are essentially immobile during the whole time interval of the IOP propagation. As a consequence, the magnitude of the transmitted wave, as well as efficiency of the IOP wave suppression, is determined mainly by the attenuation due to the (nonlinear) drag.

A. Droplet Drag by an Acoustic Wave: Crossover Droplet Size

In the simplest case, the motion of a spherical liquid droplet experiencing drag from the moving gas may be described by the equation [21,22,25]

$$m_{dr} \frac{du_{dr}}{dt} = \frac{C_D(Re_{g,dr})}{2} \rho_{gas} u_{g,dr} |u_{g,dr}| \frac{\pi d_{drop}^2}{4} \quad (1)$$

where $u_{g,dr} = u_g - u_{dr}$ is the relative velocity, and $Re_{g,dr}$ is the Reynolds number calculated for the instantaneous relative velocity of the droplet; $Re_{g,dr} = \rho_g d_{drop} u_{g,dr} / \mu_g$. Dependence of the drag coefficient C_D on the Reynolds number Re may be approximated by the following interpolation formula:

$$C_D(Re) = \frac{24}{Re} + \frac{6}{1 + \sqrt{Re}} + 0.4 \quad (2)$$

which describes very well the experimental data for water droplets [25]. According to Eq. (2), the value of $C_D(Re_{g,dr})$ varies from 2 to 0.4 within the range of droplet diameters from 10 μm to 10 mm for the gas velocities $u_g = (40\text{--}70)$ m/s (Fig. 3a).

Equation (1) implies that the droplet accelerates or decelerates by the drag depending on the sign of the relative velocity $u_{g,dr}$. For sufficiently slow change of the gas velocity (equivalently, for sufficiently long incoming wavelength), the droplet eventually attains the velocity close to the instantaneous velocity of the gas. In this limit,

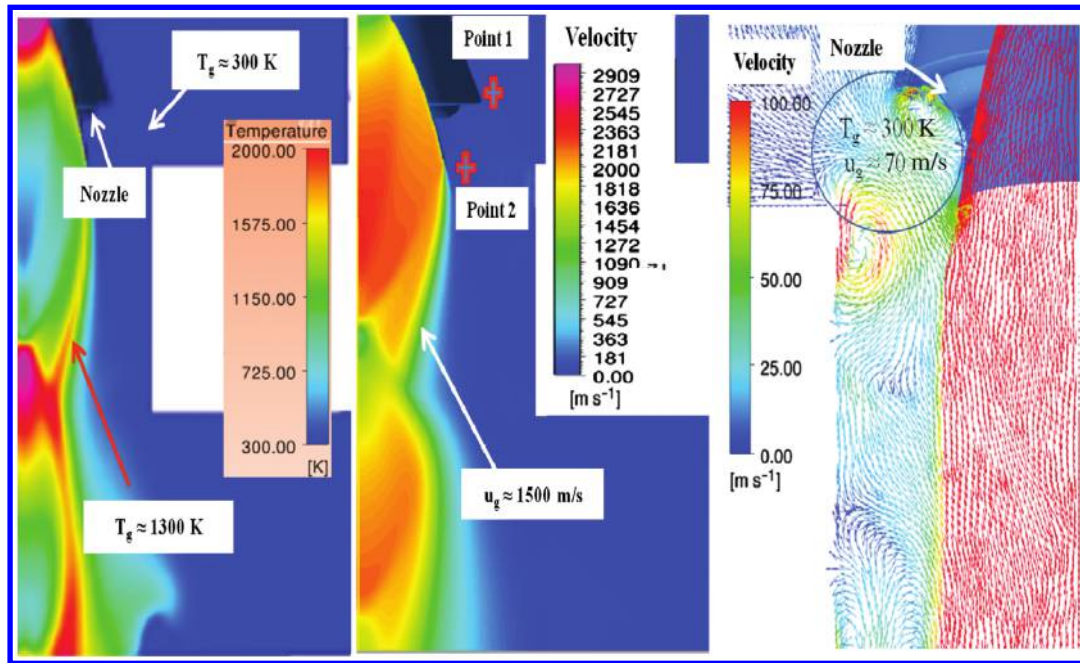


Fig. 2 Typical gas temperature and velocity fields near the nozzle and in the trench.

one can estimate the characteristic drag time τ_{drag} by assuming that the gas velocity is constant on the timescale τ_{drag} and rewriting Eq. (1) in the following form:

$$\frac{1}{u_{g0}} \frac{du_{g,dr}}{dt} = -\frac{u_{g,r}^2}{u_{g0}^2} \frac{1}{\tau(u_{g,dr})},$$

$$\tau(u_{g,dr}) \equiv \frac{4}{3C_D(Re_{g,dr})} \left(\frac{\rho_L}{\rho_g} \right) \frac{d_{\text{drop}}}{u_{g0}}, \quad \tau_{\text{drag}} \approx \tau(u_{g0}) \quad (3)$$

where u_{g0} is the characteristic gas velocity in the acoustic wave, and $Re_{g,dr}$ is the Reynolds number calculated for the instantaneous relative velocity of the droplet. Equation (3) is accurate for a sufficiently long wavelength, i.e., for $\tau_{\text{drag}} \ll \tau_{\text{pulse}}$. The estimate $\tau_{\text{drag}} \approx \tau(u_{g0})$ of the characteristic drag time can be justified by the fact that the relative velocity of the droplets is of the order of the characteristic velocity of the gas; $u_{g,dr} \approx u_{g0}$. Indeed, there are three velocity scales in the problem: $U_1 = u_{g0} \sim 70$ m/s, $U_2 = d_{\text{drop}}/\tau_{\text{pulse}} \sim 0.007$ m/s, and $U_3 = \mu_g/(d_{\text{drop}}\rho_g) \sim 0.08$ m/s, for the characteristic $\tau_{\text{pulse}} \sim 30$ ms and $d_{\text{drop}} \sim 0.2$ mm (see Sec. III.E). The corresponding Reynolds numbers are $Re(U_1) \sim 7000$, $Re(U_2) \sim 0.1$, and $Re(U_3) \sim 1$, respectively. Therefore, the scales U_2 and U_3 correspond to Stokes drag. The relaxation time τ_{drag} for the Stokes drag is $\tau_{\text{drag}} = (d_{\text{drop}})^2 \rho_L / (18\mu_g) \sim 0.110$ s, which is much larger than τ_{pulse} . Therefore, the droplets cannot accelerate to the velocity $\sim u_{g0}$ over the duration of the pulse. It follows that the scales U_2 and U_3 are irrelevant, and the relative velocity is determined by the scale U_1 , i.e., $u_{g,dr} \approx u_{g0}$. Large $R_{g,r} \sim R(u_{g0}) \sim 7000$ implies

that the drag on the droplets is nonlinear and results of the Stokes drag calculations [22] do not apply.

The condition $\tau_{\text{drag}} \ll \tau_{\text{pulse}}$ can be considered as the criterion on the droplet size to follow the gas motion. Large droplets correspond to the regime $\tau_{\text{drag}} \gg \tau_{\text{pulse}}$, where the droplets do not have time to reach the instantaneous gas velocity over the duration of the acoustic pulse τ_{pulse} . The crossover size of the droplet is determined by the condition $\tau_{\text{drag}} = \tau_{\text{pulse}}$, which is equivalent for the following implicit equation for $d_{\text{dr}}^{\text{cr}}$: [$C_D(Re)$ is $d_{\text{dr}}^{\text{cr}}$ dependent, too]:

$$d_{\text{dr}}^{\text{cr}} = \frac{3}{4} u_{g0} \tau_{\text{pulse}} \frac{\rho_{g0}}{\rho_L} C_D(Re_{g,dr}) \quad (4)$$

Aerosol with large droplets, $d_{\text{dr}} \gg d_{\text{dr}}^{\text{cr}}$ will be called *coarse aerosol* in the rest of the paper and aerosol with small droplets, $d_{\text{dr}} \ll d_{\text{dr}}^{\text{cr}}$, will be called *fine aerosol*, or simply *mist*. According to Fig. 3b, condition $\tau_{\text{drag}} \ll \tau_{\text{pulse}}$ is fulfilled for water droplets with diameter $d_{\text{drop}} \ll d_{\text{dr}}^{\text{cr}}$, where $d_{\text{dr}}^{\text{cr}} \approx 0.6$ mm for the full-scale rockets with the following parameters: $u_{g0} = (50-70)$ m/s, $T_g = 300$ K, $p = 1$ atm, and $\tau_{\text{pulse}} \approx 30$ ms.

It is assumed that the engines of the subscale model are designed to ensure that the characteristic pressures/velocities in the flow are close to those in the full-scale rocket. This corresponds to scaling the characteristic timescales of the engine transients by the lengthscales ratio. For the 5% subscale model, this implies $\tau_{\text{pulse}} \approx 1.5$ ms. In this case, the droplet crossover size is found to be $d_{\text{dr}}^{\text{cr}} \approx 60$ μm for $u_{g0} = (50-70)$ m/s (Fig. 3b). It should be noted that, because of the dependence of the drag coefficient on the droplet diameter [Eq. (2)],

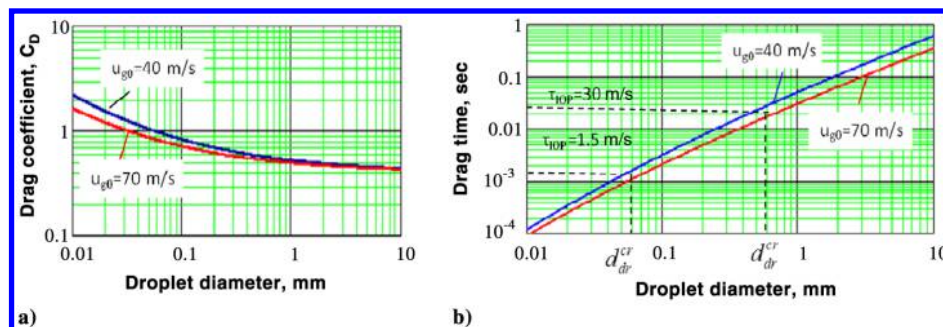


Fig. 3 Dependence of the drag coefficient and drag time of spherical water droplets on the droplet diameter.

the crossover droplet size does not scale linearly with the size of the system. Indeed, for the 5% subscale tests, the IOP timescale is decreased by a factor of 20, whereas the crossover droplet size is seen to decrease by a factor of 10 only. It then follows that an aerosol with droplets of the same diameter, e.g., $d_{dr} \approx 0.1$ mm, may appear as a mist for the full-scale rocket and as a coarse aerosol for its 5% subscale model.

In the subsequent section, it will be shown that the effects of the mist and coarse aerosol layers on the IOP wave propagation and, accordingly, their efficiencies in the IOP suppression are very different.

B. Interaction of Acoustic Waves with Fine Aerosol Layers

In the case of a mist, the condition $\tau_{drag} \ll \tau_{pulse}$ holds, i.e., that the droplets are sufficiently small and are able to follow the gas motion in the acoustic wave. As a consequence, a mist can be considered as a gaseous medium with an effective density ρ_{aer} . The sound speed c_{aer} in this case is given by Wood's formula [26]:

$$c_{aer} = \frac{c_g}{\sqrt{1-f_L}} \left(\frac{\rho_g}{\rho_{aer}} \right)^{1/2}, \quad \rho_{aer} = f_L \rho_L + (1-f_L) \rho_g \quad (5)$$

The corresponding amplitude transmission coefficient for a monochromatic acoustic wave with normal incidence is well known [21]:

$$T_{aer}^{fine} = \frac{4c_g c_{aer} \rho_g \rho_{aer}}{(c_g \rho_g + c_{aer} \rho_{aer})^2 \exp(-ik_{aer} h_{aer}) - (c_g \rho_g - c_{aer} \rho_{aer})^2 \exp(ik_{aer} h_{aer})} \quad (6)$$

where

$$k_{aer} = \frac{2\pi}{\lambda_{aer}} = \frac{2\pi\nu}{c_{aer}} = \frac{2\pi\sqrt{1-f_L}}{\lambda_g} \left(\frac{\rho_{aer}}{\rho_g} \right)^{1/2} \quad (7)$$

and $\lambda_g = c_0/\nu$ is the wavelength in air. It then follows from Eqs. (5–7) that

$$|T_{aer}^{fine}| = \left\{ \cos^2 \left(\frac{2\pi(1-f_L)bh_{aer}}{\lambda_g} \right) + a^2 \sin^2 \left(\frac{2\pi(1-f_L)bh_{aer}}{\lambda_g} \right) \right\}^{-1/2}, \quad (8)$$

$$a = \frac{b^2+1}{2b}, \quad b = \frac{1}{\sqrt{1-f_L}} \left(\frac{\rho_{aer}}{\rho_g} \right)^{1/2}$$

where both $a > 1$ and $b > 1$. Equations (6–8) are valid for weak attenuation, i.e., for $h_{aer}\alpha \ll 1$, where α is the attenuation coefficient of sound in the aerosol. In this case, the coefficient of reflection $|R_{aer}^{fine}| = 1 - |T_{aer}^{fine}|$. For $h_{aer}\alpha \gg 1$, the transmission coefficient is smaller than predicted by Eqs. (6–8). However, in the frequency range of interest for the IOP and the width of aerosol layers, $h_{aer} \sim 0.1$ m, the wavelength in the aerosol is much larger than

the width of the layer, $h_{aer} \ll \lambda_{aer}$. Therefore, $h_{aer}\alpha \gg 1$ implies $\lambda_{aer}\alpha \gg 1$, which implies that the wave is strongly reflected, and $|R_{aer}^{fine}| > 1 - |T_{aer}^{fine}|$ for $|T_{aer}^{fine}|$ as predicted by Eqs. (6–8). In the following analysis, attenuation will be neglected for the fine aerosols, meaning that the predicted reflection should be considered as a lower bound on the actual reflection. It should be noted that, for very small droplets where the Stokes drag regime applies attenuation is weak, $\lambda_{aer}\alpha \ll 1$ [22]. It can be conjectured that attenuation for mists is weak in general. In fact, the energy is transferred from the moving gas to the droplets, but this process is reversible, and the energy is then transferred from the droplets back to the gas in the course of one period of the wave. Only a small portion of the energy is lost to friction.

When $h_{aer}/\lambda_g \ll 1/b$, the formula in Eq. (8) can be further simplified to

$$|T_{aer}^{fine}| = \left[1 + \left(\frac{\pi h_{aer} \rho_{aer}}{\lambda_g \rho_g} \right)^2 \right]^{-1/2} \quad (9)$$

It should be noted that Eq. (9) with $\rho_{aer} h_{aer} = \rho_L h_L$ describes the transmission coefficient for a pure water layer of thickness $h_L < \lambda_g$ [21,27].

According to Eq. (8), the transmission coefficient in a mist depends on h_{aer}/λ_g and f_L but does not depend on the droplet diameter. It has a minimum value of $T_{min} = a^{-1}$, which is first attained at $\lambda_g = 4b(1-f_L)h_{aer}$. These formulas show that the liquid volume fraction should be sufficiently high ($T_{aer}^{fine} < 0.3$ at $f_L \geq 0.05$) in order for the aerosol to be able to have a significant mitigating effect. Also, the aerosol width h_{aer} should lie in a certain range around the optimal value $h_{aer}^{opt} = \lambda_g/4b(1-f_L) = \lambda_{aer}/4$. Figure 4a shows the transmission coefficient as a function of the relative width of the aerosol layer h_{aer}/λ_g for several values of f_L . It can be seen that the thickness of a sufficiently opaque layer falls in a rather broad range $0.01 \leq h_{aer}/\lambda_g \leq 0.04$ for $f_L = 0.15$. This parametric range is marked by the thick brown line in Fig. 4. For example, for wavelengths $\lambda_g = 10$ m ($\tau_{pulse} = 30$ ms) and $\lambda_g = 0.5$ m ($\tau_{pulse} = 1.5$ ms), these correspond to the ranges $0.1 \text{ m} \leq h_{aer} \leq 0.4$ m and $0.5 \text{ cm} \leq h_{aer} \leq 2$ cm, respectively. Such widths of the mist layers were used in the simulations (see Sec. IV). The observed resonant increase of the transmission for certain values of h_{aer} corresponds to the constructive interference effect for $h_{aer} = \lambda_{aer}/4$. This effect does not play a role in the transmission of the IOP wave through the realistic aerosol layers. First, the width of the aerosol layer varies in space. Averaging Eq. (8) over the variations can lead to a substantial decrease of the resonance spikes. Figure 4b shows a significant decrease for 10% spatial variation of the thickness, modeled by the functional dependence $h(x) = h_0[1 + 0.1 \cdot \sin(2\pi \cdot a \cdot x/\lambda_g)]$ for $\lambda_g = 10$ m. It should be noted that, in the main part of the frequency range, away from the resonances, the transmission coefficient is not affected by the 10% spatial variations. The second reason why the resonances do not effect the IOP wave transmission is that Eqs. (6–8) are obtained for monochromatic acoustic waves, whereas the IOP pulses are characterized by a finite spectral width. To calculate the transmitted pulse for $h_{aer} = 0.1$ m and $f_L = 0.15$, the transmission

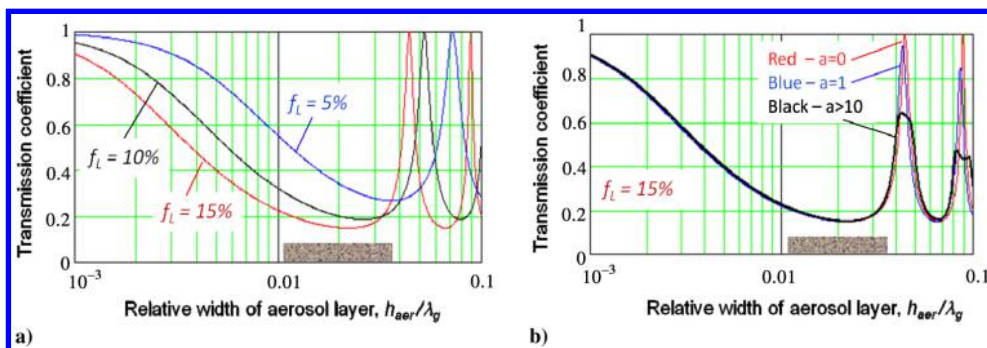


Fig. 4 Transmission coefficient for mist layers vs h_{aer}/λ_g for a) aerosol thickness $h = \text{const}$ and b) $h(x)$.

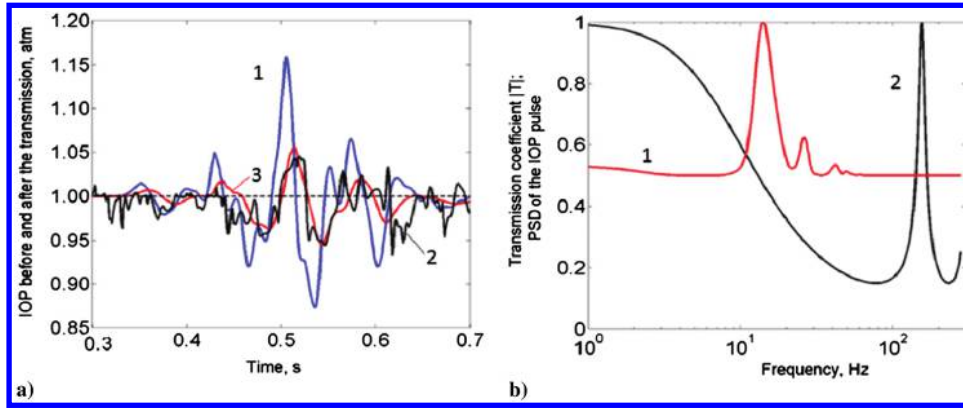


Fig. 5 a) The incident (curve 1) and transmitted IOP pulses obtained numerically (curve 2) and theoretically (curve 3), and b) transmission coefficient and PSD.

coefficient in Eq. (6) for $h_{\text{aer}} = 0.1$ m and $f_L = 0.15$ is convoluted with the Fourier transform of the transmitted pressure wave, taking as the incident wave the pressure time trace from the ANSYS simulation of the IOP at point 1. Figure 5a shows the incident (curve 1) and the transmitted IOP wave obtained from the ANSYS simulations with droplets (curve 2) and theoretically (curve 3), using the transmission coefficient of an appropriate mist layer. Also, Fig. 5b shows the power spectrum density (PSD) of the incident wave (curve 1) and the modulus of the Fourier transform of the transmission coefficient given by Eq. (6) (curve 2). From this figure, one can see that most of the energy of the wave is concentrated in the part of the spectrum that is efficiently suppressed by the aerosol layer. Therefore, the resonance spikes seen in Fig. 5 do not play a significant role for the suppression of the IOP pulses. Figure 5a shows that the calculated transmitted IOP wave shifts in time with respect to the incoming IOP wave and has the amplitude reduced by a factor of three. This theoretical prediction shows an excellent agreement with the result of the ANSYS simulation for the same mist parameters and $d_{\text{drop}} = 0.25$ mm (see Sec. IV for details). From Fig. 5b, it appears that the parameters of the aerosol can be changed leading to an even stronger suppression if the first minimum of the transmission, attained at $\lambda_g = 4b(1 - f_L)h_{\text{aer}}$, is tuned to correspond to the spectral maximum of the pulse ν_{pulse} . In practice, the tuning parameters can be either f_L or h_{aer} , and their optimal value is determined by the relation $c_g/\nu_{\text{pulse}} = 4b(1 - f_L)h_{\text{aer}}$.

C. Interaction of Acoustic Waves with the Coarse Aerosol Layers

The acoustic wave is attenuated by the aerosol layer due to the drag between the droplet and the moving gas. For coarse aerosol, where $\tau_{\text{drag}} \gg \tau_{\text{pulse}}$, and for small attenuation, the amplitude of the transmission coefficient for the wave passing normally through an aerosol layer of thickness h_{aer} can be calculated. First, a heuristic derivation of the attenuation coefficient will be presented based on simple physical considerations. Next, a more detailed analysis will follow, aiming to assess the quality of approximations involved.

The motion of the droplets caused by an acoustic wave of frequency ν can be neglected for $\tau_{\text{drag}}\nu \gg 1$. If, in addition, the attenuation on the scale of the wavelength is small (i.e., $\lambda_{\text{aer}}\alpha_{\text{aer}} \ll 1$ holds), the wave propagating in the aerosol can be considered a traveling plane wave. The flow near the droplets can be considered as quasi stationary for frequencies typical to the IOP. The time-averaged energy flux of a traveling plane wave is $J = \rho_g < u_g^2 > c_{\text{aer}}$, where c_{aer} is the sound velocity in the aerosol, u_g is the velocity of gas in the wave, and the brackets denote time averaging. The time-averaged power spent on drag in an infinitesimal aerosol layer of width δx and unity area is $\delta P = < u_{g,\text{dr}} F_{\text{drag}}(u_{g,\text{dr}}) > \delta N$, where F_{drag} is the drag force per droplet, $u_{g,\text{dr}}$ is velocity of a droplet relative to the ambient gas, and the number of droplets in the infinitesimal layer is $\delta N = f_L \delta x / (4/3\pi R^3)$. In the leading order in $(\tau_{\text{drag}}\nu)^{-1}$, and for initially stationary droplets, $u_{g,\text{dr}} = u_g$. Equating $\delta P = \delta J$ leads to

the following ordinary differential equation for the spatial variation of the time-averaged variables:

$$\begin{aligned} \rho_g c_{\text{aer}} \delta \langle u_g^2 \rangle &= - \langle u_g F_{\text{drag}}(u_g) \rangle n_{\text{drop}} \delta x, \\ \frac{d \langle u_g^2 \rangle}{dx} &= - \frac{n_{\text{drop}}}{\rho_g c_{\text{aer}}} \langle u_g F_{\text{drag}}(u_g) \rangle, \\ n_{\text{drop}} &\equiv \frac{3f_L}{4\pi r_{\text{drop}}^3} \end{aligned} \quad (10)$$

Equation (10) can also be obtained in the linear acoustic approximation from the equations of motion for the gas and droplets. The continuity equation and the momentum equation for the gas in the acoustic limit become

$$\partial_t p' + \rho_g c_g \partial_x u_g = 0 \quad \rho_g \partial_t u_g + \partial_x p' = -n_{\text{drop}} F_{\text{drag}}(u_g) \quad (11)$$

where $u_{g,\text{dr}} = u_g$ has been taken in the leading order in $(\tau_{\text{drag}}\nu)^{-1}$. Retaining the force term in Eq. (11) in the acoustic approximation is valid, provided the nonlinear corrections are still smaller. The dropped terms to Eq. (11) are of the order of $\rho_g u^2 / \lambda_{\text{aer}}$, therefore retaining the drag term is valid if

$$|n_{\text{drop}} F_{\text{drag}}(u_g)| \gg \rho_g u_g^2 / \lambda_{\text{aer}} \quad (12)$$

Next, Eq. (11) can be used to derive the following partial differential equation for the acoustic energy flux $j = p' u_g$:

$$\partial_x (p' u_g) = u_g F_{\text{drag}}(u_g) n_{\text{drop}} - \frac{\rho_g^{-1} c_g^{-2}}{2} \partial_t (p')^2 - \frac{\rho_g}{2} \partial_t u_g^2 \quad (13)$$

Since the time derivatives in Eq. (13) act on functions that are bounded, averaging this equation over a sufficiently long time interval eliminates the last two terms, yielding

$$\frac{d \langle p' u_g \rangle}{dx} = n_{\text{drop}} \langle u_g F_{\text{drag}}(u_g) \rangle \quad (14)$$

Under the assumption of small attenuation, the wave in the aerosol can be approximated by the traveling plane wave, for which $p' = \rho_g u_g c_{\text{aer}}$ holds. Inserting this expression into Eq. (14) brings it to the form of Eq. (10), obtained on heuristic grounds. In the fully turbulent flow regime, which is relevant for the IOP, $F_{\text{drag}}(u_g) = -(1/2) C_D \pi r_{\text{drop}}^2 \rho_g |u_g| u_g$, with $C_D \approx 0.4$. The validity condition [Eq. (12)] translates into $d_{\text{dr}} \ll (3/4) \lambda_{\text{aer}} f_L C_D$ or $d_{\text{dr}} \ll 50$ cm in the parametric regime of interest for the full-scale rocket, which is obviously satisfied by droplets in any water spray system. Equation (10) takes the following form:

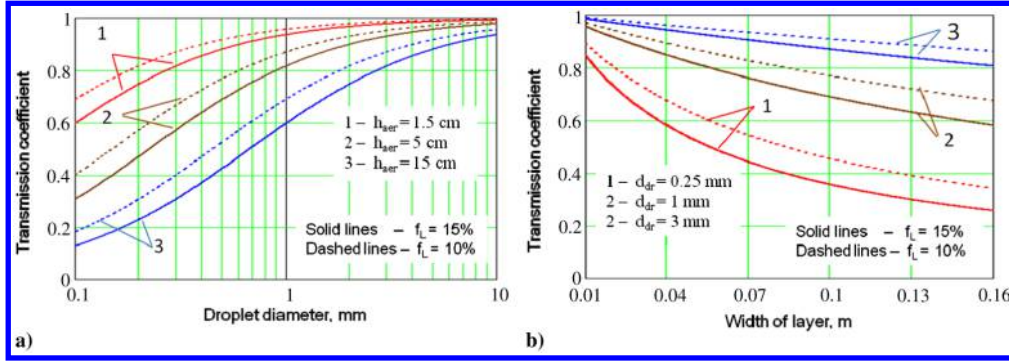


Fig. 6 Transmission coefficients for coarse aerosol layers vs a) droplet diameter and b) the width of the aerosol layer, for $u_g/c_0 = 0.2$.

$$\frac{d\langle u_g^2 \rangle}{dx} = -\frac{3C_D f_L}{4d_{\text{drop}} c_{\text{aer}}} \langle |u_g| u_g^2 \rangle \quad (15)$$

For a monochromatic traveling wave with slowly varying amplitude, $u_g = u_0(x) \sin(2\pi\nu t - x/c_{\text{aer}} + \varphi)$, the time averaging gives $\langle u_0^2 \rangle(x) = u_0(x)^2/2$ and $\langle |u_g| u_g^2 \rangle(x) = 4/(3\pi)u_0(x)^3$, leading to

$$\frac{du_0(x)}{dx} = -\frac{(u_0(x))^2 f_L C_D}{\pi d_{\text{drop}} c_{\text{aer}}} \Rightarrow u_0(x) = \frac{u_{g0}}{1 + \alpha x},$$

$$T_{\text{aer}}^{\text{coarse}}(x) = (1 + \alpha x)^{-1}, \quad \alpha \equiv \frac{C_D f_L u_{g0}}{\pi d_{\text{drop}} c_{\text{aer}}} \quad (16)$$

where u_{g0} is the initial amplitude of the wave, and α is the attenuation coefficient. Note that the considered attenuation mechanism is fundamentally nonlinear in the amplitude of the incident acoustic wave and is related to the onset of turbulent gas motion in the vicinity of each droplet upon passage of the wave. The value of $T_{\text{aer}}^{\text{coarse}}$ does not depend on the acoustic wave frequency ν but varies with the droplet diameter d_{drop} and the maximum gas velocity u_{g0} of the wave. It should be noted, however, that for smaller diameters, the frequency of the acoustic wave has to be greater in order to satisfy the condition $\tau_{\text{drag}}\nu \gg 1$ required for Eq. (16) to be valid. Small attenuation is yet another assumption for the derivation. It means $\lambda_{\text{aer}}\alpha \ll 1$. Using the expression for α in Eq. (16), one can obtain

$$\lambda_g \alpha \ll 1 \Rightarrow \frac{4\eta_{\text{aer}}}{3\pi\tau_{\text{drag}}\nu} \ll 1, \quad \tau_{\text{drag}} \equiv \frac{4\rho_L d_{\text{drop}}}{3C_D \rho_g u_{g0}}, \quad \eta_{\text{aer}} \equiv f_L \frac{\rho_L}{\rho_g} \quad (17)$$

where $\eta_{\text{aer}} \gg 1$ is the mass loading of aerosol for $f_L \ll 1$. It should be noted that inequality [Eq. (17)] implies not only that attenuation is small but also that reflection is small. Indeed, since $\lambda_{\text{aer}}\alpha \ll 1$, reflection can be substantial only if the impedance mismatch between the aerosol layer and air is large. For essentially immobile droplets, the impedance and the sound velocity cannot depend on the droplet density ρ_L . Therefore, the impedance mismatch and deviation of the sound velocity c_{aer} from the ambient sound velocity c_g are functions of $\eta_{\text{aer}}/(\tau_{\text{drag}}\nu)$ and f_L : the only dimensionless parameters independent of ρ_L . As a consequence, for $\eta_{\text{aer}}/(\tau_{\text{drag}}\nu) \ll 1$ and $f_L \ll 1$, the impedance mismatch is negligible and $c_{\text{aer}} \approx c_g$. It can be concluded that inequality [Eq. (17)] implies both small attenuation and small reflection. The sound velocity c_{aer} in the expression of Eq. (16) for α can be replaced by the ambient sound velocity c_g to the leading order in $\eta_{\text{aer}}/(\tau_{\text{drag}}\nu)$. This substitution is employed in what follows. Equation (17) implies that attenuation and reflection are small for sufficiently large droplets:

$$d_{\text{drop}} \gg d_{\text{drop}}^* = \frac{f_L C_D u_{g0}}{\pi\nu} = \lambda_g \frac{f_L C_D u_{g0}}{\pi c_g} \quad (18)$$

For $C_D = 0.4$, $f_L = 0.15$, and $u_{g0}/c_g = 0.2$, the reflection can be neglected for $d_{\text{drop}} \gg 0.004\lambda_g$. For $\lambda_g = 10$ m, as in the full-scale

rocket, the reflection can be neglected for $d_{\text{drop}} \gg 4$ cm. The bound 4 cm exceeds the typical size of the droplet in the water jet even before the breakup (see Sec. III.E). Therefore, the reflection in the full-scale rocket cannot be neglected for a sufficiently wide aerosol layer. On the other hand, for the 5% subscale model, the IOP wavelength $\lambda_g \approx 0.5$ m, and reflection can be neglected for $d_{\text{drop}} \gg 2$ mm. Since, as explained in Sec. III.E, the breakup is negligible during the IOP pulse for the 5% subscale model and the typical initial size of the droplets in the water jet is ~ 1 cm, the reflection can be neglected for the subscale model. In addition, it is important to note that, for the typical $h_{\text{aer}} \sim 0.1$ m for the full-scale model and $h_{\text{aer}} \sim 1$ cm for the subscale model and the frequency range of interest for the IOP, $h_{\text{aer}} \ll \lambda_{\text{aer}}$. Therefore, even for smaller droplets where the strong inequality $\lambda_{\text{aer}}\alpha \ll 1$ [or, equivalently, Eq. (18)] does not hold, the condition $h_{\text{aer}}\alpha \ll 1$ is still satisfied and attenuation and reflection are expected to be small, possibly even for $d_{\text{drop}} \sim d_{\text{drop}}^* \cdot h_{\text{aer}}/\lambda_{\text{aer}}$, i.e., for $d_{\text{drop}} \sim 0.4$ cm for the full-scale rocket and $d_{\text{drop}} \sim 0.2$ mm for the 5% model. The dependencies of the transmission coefficient $T_{\text{aer}}^{\text{coarse}}$ given by Eq. (16) on aerosol parameters are presented in Fig. 6 (also see Sec. III.D). As noted previously, in the case under consideration, $v_g \leq 70$ m/s (see Fig. 2), i.e., $u_{g0}/c_g \leq 0.2$. Therefore, the curves in Fig. 6 corresponding to the transmission coefficient given by Eq. (16) display a lower bound on the actual value of $T_{\text{aer}}^{\text{coarse}}$.

The transparency of the coarse aerosol layers increases, i.e., the layer absorbs the wave less efficiently when the droplet diameter increases (Fig. 6a) or the layer thickness decreases (Fig. 6b). The condition $\tau_{\text{drag}} \gg \tau_{\text{pulse}}$ for $u_{g0}/c_g \leq 0.2$ can be fulfilled for $d_{\text{drop}} > 2.5$ mm for the full-scale model and for $d_{\text{drop}} > 0.25$ mm for the 5% subscale model (Fig. 6). The presence of polydispersity is expected to increase the transparency of coarse aerosols. Indeed, for coarse aerosol layers, the transmission coefficient can be calculated based on Eq. (16), in which the attenuation α coefficient should be averaged over the distribution $f(D)$ of the droplet diameters D :

$$\alpha \rightarrow \int_0^{\infty} \alpha f(D) dD \quad (19)$$

Consider, for example, the lognormal distribution [assuming that $\tau_{\text{drag}} \gg \tau_{\text{pulse}}$ or, equivalently, that $D \gg d_{\text{dr}}^*$ for most droplets, where d_{dr}^* is given by Eq. (4)] with median diameter \bar{D} and relative width σ (for a recent overview of different polydispersity models, see, e.g., [28]):

$$f(D) = \frac{1}{D\sigma\sqrt{2\pi}} \exp\left[-\frac{1}{2}\left(\frac{\ln(D/\bar{D})}{\sigma}\right)^2\right] \quad (20)$$

The most likely value of the droplet diameter in this distribution is equal to $\bar{d}_{\text{drop}} = \bar{D}e^{-\sigma^2}$. Direct integration of Eq. (8) using the expression in Eq. (16) for α yields

$$\alpha \equiv \frac{3C_D f_L u_{g0}}{8\bar{d}_{\text{drop}} c_g} e^{-\sigma^2/2} \quad (21)$$

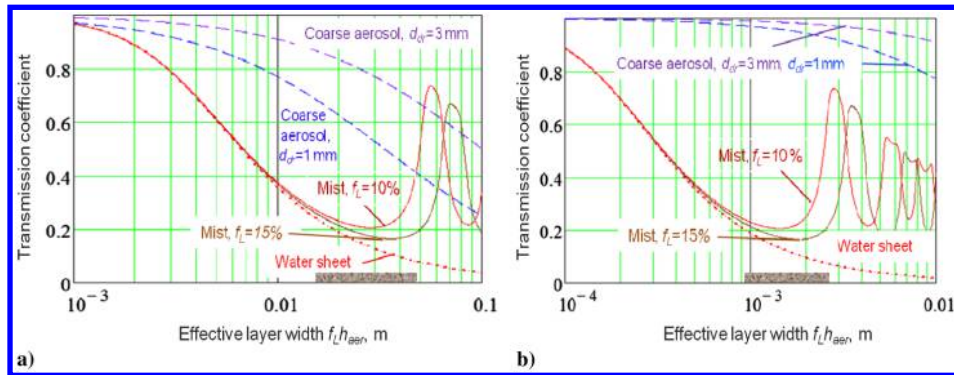


Fig. 7 Transmission coefficients for water and aerosol layers vs $f_L h_{aer}$ for acoustic wavelengths a) $\lambda_g = 10$ m and b) $\lambda_g = 0.5$ m.

One can see that, for a fixed value of \bar{d}_{drop} , the attenuation coefficient decreases with σ , which is a measure of the polydispersity of the aerosol. Therefore, in the considered case, polydispersity reduces the ability of the aerosol to absorb the incoming IOP wave. The best mitigation in this regime is then achieved with the smallest possible droplets ($\bar{d}_{drop} \approx d_{dr}^{cr}$), for which the distribution is sharply peaked.

D. Dependencies of the Transmission Coefficient on Aerosol Density and Wave Frequency

The dependencies of the transmission coefficient for aerosol and pure water layers on the effective liquid layer width $f_L h_{aer}$ obtained from Eqs. (7–9, 16) are presented in Fig. 7. As can be seen from Fig. 7, the optimal value of $f_L h_{aer}$ for mist satisfies the following conditions: $15 \text{ cm} \leq f_L h_{aer} \leq 50 \text{ cm}$ for $\lambda_g = 10$ m (Fig. 7a) and $0.7 \text{ mm} \leq f_L h_{aer} \leq 2.5 \text{ mm}$ for $\lambda_g = 0.5$ m (Fig. 7b). These parameter ranges are marked by the thick brown lines in Fig. 7. As explained in Sec. III.B, following Eq. (8), such mist layers are expected to efficiently reflect IOP waves. Similarly, according to Eq. (9) for $f_L = 1$, a pure water sheet would reflect these acoustic waves equally well. It should be noted, however, that thin water sheets quickly become spatially unstable: first developing undulations and then breaking up into large blobs [29,30]. As a consequence, the disintegrating water sheet is expected to become transparent to the IOP waves.

As follows from the discussions after Eqs. (16) and (6–9), for the typical $h_{aer} \alpha \ll 1$, layers of aerosol with large droplets (coarse aerosols) are more transparent at higher frequencies than layers of mist for the same width and liquid fraction (Fig. 8). The transparency of the coarse aerosol layers does not depend on the acoustic wave frequency, as implied by Eq. (16), but is a function of the droplet size. Conversely, the transparency of the mist layers does not depend on the size of the droplets but is strongly frequency dependent [see Fig. 4 and Eqs. (6–9) with frequency $\nu = c_g/\lambda_g$]. Note that the smallness criterion $\tau_{drag} \ll 1$ depends on both the droplet diameter and on the parameters of the wave, such as frequency and amplitude u_{g0} . This makes the frequency dependence of the transmission coefficient for aerosol layers rather complex. It can be given explicitly only for

relatively low- or high-frequency ranges where the conditions $\tau_{drag} \ll 1$ or $\tau_{drag} \gg \eta_{aer}$ are valid and Eqs. (8) and (16) can be used, respectively. These dependencies for relatively thin aerosol layers $h_{aer} \ll \lambda_{aer}$ are presented in Fig. 8, where we used Eq. (8) for $\ll 0.25\tau_{drag}^{-1}$ and Eq. (16) for $\gg 4\tau_{drag}^{-1}$. The dashed lines in Fig. 8 join the curves for these two frequency ranges. Curves 1–5 in Fig. 8a correspond to droplet diameters equal to 5, 3, 1, 0.2, and 0.1 mm, respectively. Curves 1–5 in Fig. 8b correspond to droplet diameters equal to 1 mm, 0.2 mm, 0.1 mm, and $50 \mu\text{m}$, respectively. The values of the liquid fraction f_L , the width of the layer h_{aer} , and gas velocity v_g are shown in the figures. Figure 8a essentially describes the situation for large rockets (e.g., with typical frequency $\nu \approx \frac{1}{\tau_{pulse}} \approx 33$ Hz; see Sec. II), and Fig. 8b refers to their subscale models (with the frequency $\nu \approx \frac{1}{\tau_{pulse}} \approx 660$ Hz). Figure 8a (curve 4) shows that aerosol layers of width $h_{aer} \sim 0.1$ m for droplets of diameter

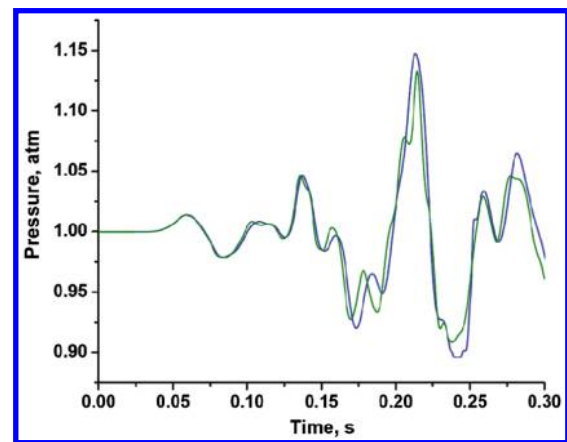


Fig. 9 Pressure time traces near the nozzle exit at point 1 for the axisymmetric geometry (blue line = 5 deg sector; green line = 180 deg sector).

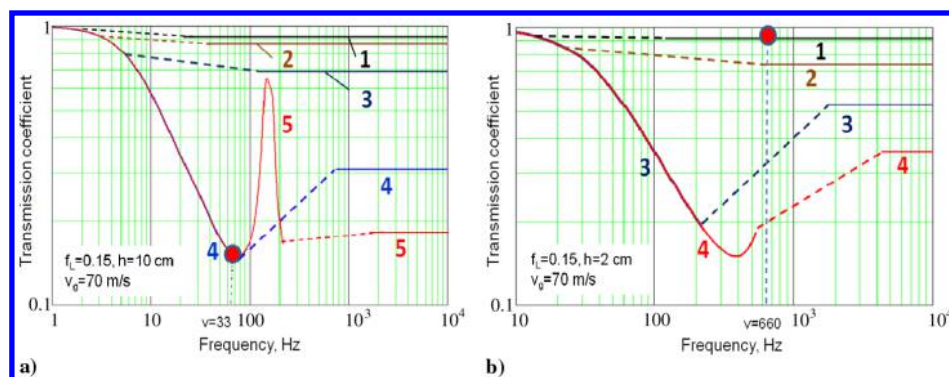


Fig. 8 Transmission coefficient for aerosol layers vs frequency of acoustic waves.

~ 0.2 mm may be effective IOP mitigators for full-scale rockets. During the full-scale rocket ignition, water droplets of diameter ~ 0.2 mm are created by the breakup of the large droplets [of $\sim (5\text{--}10)$ mm] initially present in the water spray by the acoustic wave (see next section). From the standpoint of the aerosol–wave interaction, the 0.2 mm droplets correspond to the mist for the full-scale rockets. In subscale models, the large droplets of the water spray do not have enough time to breakup to 0.2 mm. Since even for 0.2 mm the transmission is very high for the subscale model (Fig. 8b), aerosol layers of $\sim 1\text{--}2$ cm width are essentially transparent for the waves in small rockets. Droplets of diameter $d_{\text{drop}} \leq 50 \mu\text{m}$ (curve 4 in Fig. 8b) correspond to mist for $\sim 5\%$ subscale models.

The aerosol layers with such droplets will efficiently reflect the acoustic waves when the width of the layer is $h_{\text{aer}} \sim 0.5$ cm or larger. It should be stressed that the crossover droplet diameters do not scale with the size of the rocket, as mentioned in Sec. III.A. Therefore, in order to experimentally test the efficiency of IOP suppression by mist layers in a 5% subscale model, one needs to use atomized sprays with smaller droplets of diameter $d_{\text{drop}} < 50 \mu\text{m}$ to comply with the condition of Eq. (4).

E. Droplet Breakup by Acoustic Waves

Droplet breakup is an extremely complex process and its detailed understanding is still lacking despite many experimental, theoretical, and numerical studies [31–42]. Several models and approaches are available to give a basic characterization of droplet breakup as a function of the Weber number [30–34]. Under the conditions relevant for the present study, the Weber number $We > 100$ for the droplets of sizes larger than 0.25 mm in diameter and gas velocity $u_g \cong 70$ m/s in the IOP wave. Therefore, droplet breakup should be dominated by the bag breakup mechanism [39–41] that has been studied in detail numerically in the recent work [38]. In this regime, the Taylor analogy breakup model [33] may be used to estimate the minimum radius r_{min} of the breaking droplets and the breakup time τ_{break} . This model was used in the studies of [15] and is implemented in the ANSYS code. According to the Taylor model, droplet breakup occurs when the variable Y obeys the equation

$$\frac{d^2 Y}{dt^2} + \frac{20\mu_g}{\rho_L d_{\text{drop}}^2} \frac{dY}{dt} = \frac{8\rho_g u_g^2}{3\rho_L d_{\text{drop}}^2} - \frac{64\sigma Y}{\rho_L d_{\text{drop}}^3} \quad (22)$$

As follows from Eq. (22), the value of Y may exceed unity when the droplet diameter satisfies the condition

$$We = \frac{\rho_g u_g^2 d_{\text{drop}}}{\sigma} > 12 \Leftrightarrow d_{\text{drop}} > d_{\text{min}} = \frac{12\sigma}{\rho_g u_g^2} \quad (23)$$

For several values of the parameters and $p = 1$ atm, the minimum droplet diameter may be estimated to be $d_{\text{min}} \approx 0.2$ mm at $V_g = (60\text{--}70)$ m/s, $T_g = 300$ K and $d_{\text{min}} \approx 2 \mu\text{m}$ at $V_g = 1500$ m/s, $T_g = 1300$ K. The physical interpretation of the condition in Eq. (23) is as follows: breakup occurs when the dynamic gas pressure drop on the droplet is greater than the pressure drop due to surface tension. According to Eq. (22), due to the smallness of the value of $5\mu_g/\rho_L r_{\text{drop}}^2$, the lower bound on the droplet breakup time for $We > 12$ may be estimated as follows:

$$\frac{d^2 Y}{dt^2} \approx \frac{8\rho_g u_g^2}{3\rho_L d_{\text{dr}}^2} \Rightarrow \tau_{\text{deform}} = C\tau, \quad \tau = \frac{d_{\text{dr}}}{u_g} \sqrt{\frac{\rho_L}{\rho_g}}, \quad C = \sqrt{3} \quad (24)$$

The lower bound can be thought of as the characteristic time of the critical deformation of the droplet. According to the Schmehl’s model [38–40], which is based on the experimental findings of Hsinag et al. [35], the formula in Eq. (24) can describe the upper bound τ_{break} on the breakup time as well, provided the value of constant C is $C_{\text{break}} = 0.766(We - 12)^{0.25}$. For $d_{\text{drop}} = 5$ mm and $v_g = 70$ m/s the coefficient $C_{\text{break}} \approx 3$ and $\tau_{\text{break}} \approx 7$ ms. For $\tau_{\text{pulse}} \approx 30$ ms $\gg \tau_{\text{break}}$, a considerable fraction of the droplets with radii $d_{\text{drop}} \gg d_{\text{min}}$ will be broken up to the minimum radius $d_{\text{min}} \approx 0.2$ mm given by

Eq. (23). This droplet size corresponds to fine aerosol for the full-scale rocket. Therefore, the reflection of the IOP wave is large (see Sec. III.D). As a consequence, the reflection is large for the water sprays of the full-scale rocket. On the other hand, the breakup may be negligible for the 5% subscale model where $\tau_{\text{pulse}} < 1.5$ ms. As a consequence, the IOP will not reflect from the water spray in the 5% subscale model (see Sec. III.D). It should be noted that the evaporation of 0.2 mm droplets is negligible in the timeframe of interest for the region outside the plume, since the temperature of the air is close to the droplet temperature $T_L \approx 300$ K. Inside the plume, the droplets will break up on the timescale $\tau_{\text{break}} < 0.4$ ms into droplets with a diameter of $2.2 \mu\text{m}$, which evaporate very quickly ($\tau_{\text{evap}} = 10 \mu\text{s}$) due to the high temperature and velocity of the gas inside the plume ($T_g = 1300$ K and $u_g = 1500$ m/s; Fig. 2). These estimates are fully supported by the results of the ANSYS simulations (see Sec. IV).

IV. Computational Approach

CFD simulations of IOP reported in this paper were carried out using the commercial software ANSYS CFX 14.5, which employs an implicit element-based finite volume method. The simulations were performed for a simplified geometry of the exhaust hole, which captures the main features of the exhaust hole used in the space shuttle launch pad.

A. Geometry

The geometry of the exhaust hole and the nozzle was constructed using ANSYS Design Modeler. The geometry was axisymmetric. Two different approaches to the simulation were compared. First, three-dimensional (3-D) simulations were performed on a 5 deg sector and extrapolated to the full domain by rotation. Second, the results were compared to the results of 3-D simulations for 180 deg sectors in a number of cases. No appreciable difference was found (see Fig. 9). Therefore, the 3-D simulation of 5 deg sectors has been pursued in what follows to reduce the grid size and the computational time.

B. Grid Generation and Convergence Study

An unstructured grid was generated with ANSYS CFX-MESH, illustrated in Fig. 10. In most of the simulations, a mesh consisting of 2,303,963 tetrahedra and 1,097,070 wedges (a total of 3,501,063 cells and 1,008,137 nodes) was used. For the convergence study, a mesh with 6 million cells was used. The typical grid structure is shown in Fig. 10.

The mesh at the near-wall region of the nozzle required the elements to have high aspect ratios. The number of the inflated layers was taken to be 30, as shown in Fig. 10. The thickness of the first layer was 0.1–0.5 mm and the expansion factor was taken to be 1.1, corresponding to the value of $y+ < 4$ in our simulations.

The requirements for the mesh quality are primarily dictated by a sufficiently high accuracy with a minimum computational cost. Convergence was obtained by successive refinements of the critical regions to make the results essentially independent of the mesh quality. Figures 11 and 12 show the results of a convergence study, where the pressure time traces in the critical regions were compared for the meshes with 3.5 million and 6 million cells, corresponding to the minimal cell sizes of 1 and 0.5 mm, respectively, away from the boundary layers.

The aforementioned mesh refinement yields no significant difference in the pressure time traces, whereas the computational cost increases enormously. Therefore, a 3.5-million-cell mesh was used in all the simulations reported in this paper.

C. Gas Dynamics Boundary and Initial Conditions

The computational domain is shown in Figs. 10 and 12. The domain was taken to be sufficiently large to avoid any interference from the computational boundaries on the timescales of interest. For the inlet boundary condition, prescribed plenum stagnation pressure and temperature time traces were used. The “opening” (far field)

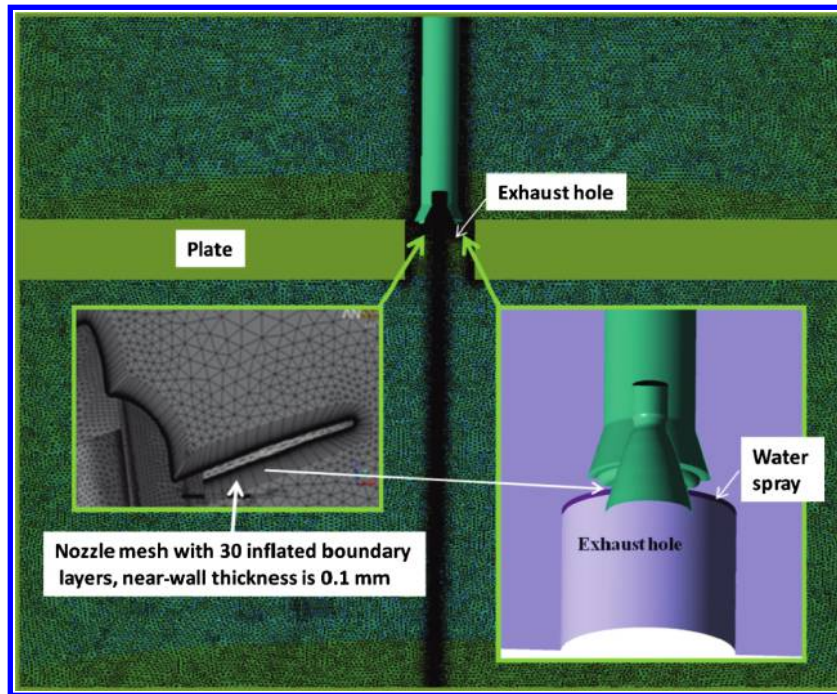


Fig. 10 Example of a computational mesh.

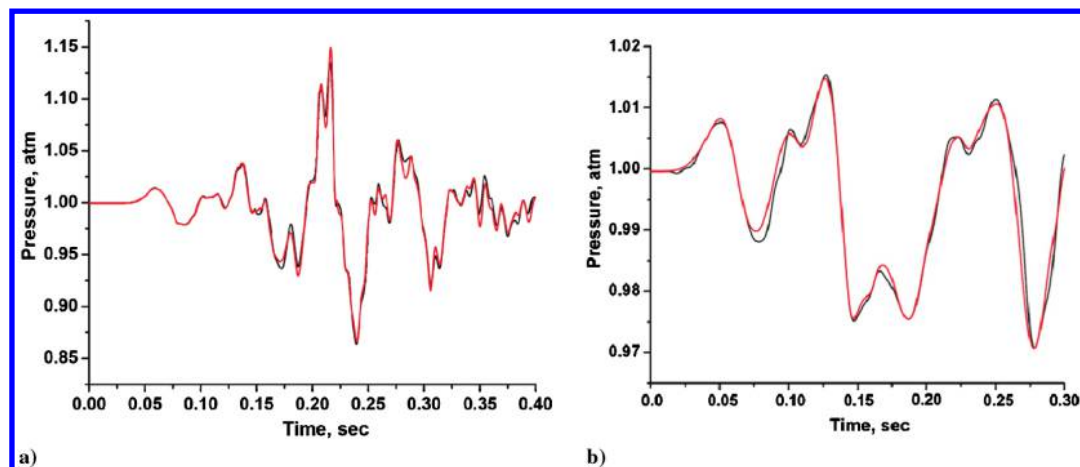


Fig. 11 Comparison of IOP at the point 1 for different grid sizes (black – 3.6 M; red – 6 M): a) no spray, and b) with spray; $d_{\text{drop}} = 0.1$ mm.

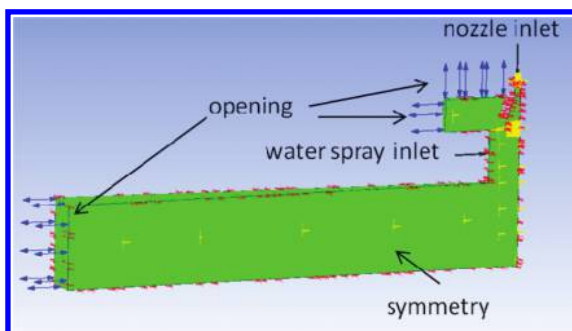


Fig. 12 Computational domain and boundary condition.

boundary conditions away from the nozzle were defined by the fixed ambient pressure of 1 atm and temperature of 300 K. The initial conditions for the air in the computational domain were 1 atm and 300 K. For the boundary condition on the wall, the adiabatic no-slip condition was employed. The exhaust gas was modeled as an ideal gas with the parameters of air.

D. Water Inlet Boundary and Initial Conditions

The injection velocity of the water droplets was taken to be 10–15 m/s, the initial droplet diameter was 0.1–3 mm, and the mass flow rate of the liquid phase was 10–30 kg/s in various simulations. Injection of the water droplets started 0.3 s before the ignition in all simulations.

E. Fluid Models

Fluid models were chosen based on the recommendations in the CFX-14.5 documentation. The computations contain two phases: the gas phase (continuous) and the liquid droplet phase (discrete). The continuous phase and the droplets are modeled by a two-way-coupled Euler–Lagrange approach, where the particle–fluid interactions are taken into account but the inelastic collisions between particles are neglected. The two-way coupling makes it possible to describe the transport of the vapor from the droplets to the gas phase. An unsteady Reynolds-averaged Navier–Stokes (URANS) simulation was carried out using the $k-\omega$ shear stress transport (SST) turbulence model. The total energy heat transfer model was chosen to include the effects of the kinetic energy for heat transfer. The density difference buoyancy

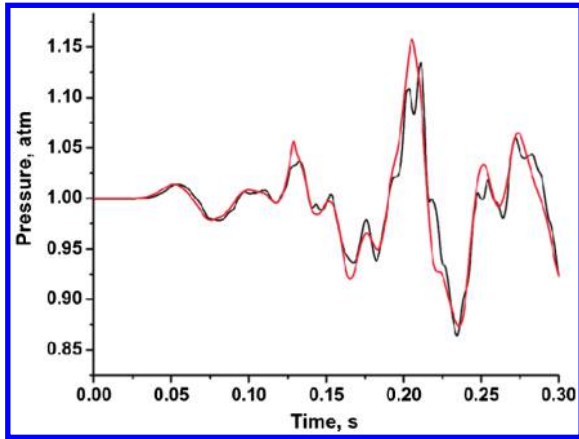


Fig. 13 Comparison of the pressure time traces near the nozzle exit at monitor point 1 for an axisymmetric geometry with time steps of 0.001 s (red curve) and 0.0001 s (black curve).

model was applied to the water droplets, and the Schiller–Naumann model was used to describe the drag. Droplet breakup, evaporation, and momentum exchange with the gas phase were taken into account. For the heat transfer during evaporation, the Ranz–Marshall model was used. The mass transfer rate for a single droplet was computed using the liquid evaporation model. The model used two mass transfer correlations, depending on whether the droplet was above or below the boiling point. The boiling point was determined through the Antoine equation. The mass transfer from the droplet was determined by the latent heat of evaporation.

F. Code Validation, Solver Control, and Convergence Studies

The ANSYS CFX software has been validated for applications to supersonic flows and multiphase flows, as used in the present work. For supersonic flow code validation see, e.g., [43–46] and the validation cases VMFL060 and VMFL037 in the ANSYS manual [43]. For the SST turbulence model and URANS validation cases, see [47,48] and VMFL045, VMFL058, VMFL036, VMFL032, and VMFL031 in the ANSYS manual [43]. For validation of the multiphase code see [49,50].

The simulations were performed in the transient mode using a high-resolution advection scheme. The numerical approximation of the time derivatives was achieved by means of a second-order backward Euler scheme.

A first-order scheme was used to model turbulence. As the convergence criterion, a rms with the 5×10^{-5} target for the residuals was set. The maximum number of coefficient loop iterations was set to 10.

The following time-step convergence study was carried out to determine the effect of the step size on the accuracy of the simulations. First, the simulation was run using a time step of 0.001 s, which is much smaller than the smallest relevant physical timescale of the problem, which is about 0.01 s. Next, the simulation was repeated using a 0.0001 s time step, and the results were compared. No appreciable differences in the simulation results were found (see Fig. 13). As a consequence, the 0.001 s time step was used in all the simulations reported.

V. IOP Mitigation by Aerosol Sprays

The efficiency of IOP suppression by aerosol layers depends on the properties of the IOP pulse, the geometry of the exhaust hole and the nozzle, and the location and the parameters of the aerosol sprays. The estimates obtained in Sec. III were used to guide the ANSYS simulations of the following tests. Water aerosols with various droplet diameters d_{dro} , liquid volume fractions f_L , and fixed velocities v_{drop} were injected from various locations. A quasi-steady droplet distribution was established within 0.3 s. At that moment, ignition set off in the SRB, which was modeled by modulation of the plenum boundary conditions in the nozzle based on the typical total pressure and total temperature time traces for the space shuttle SRB. Formation of the main IOP spikes (Fig. 1) is driven by different mechanisms, depending on the design of the nozzle and the trench, as well as on the gas pressure and temperature profiles in the SRB combustion chamber. In particular, formation of relatively large IOP spike 1 near the nozzle was associated with diffraction of the first wave (see Sec. II) on the nozzle lip. Other spikes were associated with the IOP waves originating near the bottom of the exhaust hole and the deflector (see Sec. II). Therefore, in contrast to the other spikes, spike 1 could not be reduced by the aerosol streams located below the nozzle exit. Moreover, as noted in Sec. II, the main component of the descending wave propagated downward from the nozzle exit. Therefore, it would reflect from the aerosol or water streams located below the nozzle exit. The reflected wave will propagate in the upstream direction, creating a hazard for the vehicle. The amplitude of the reflected wave is expected to be considerably larger than the amplitude of the diffracted wave in the case of a complete reflection. The results of the ANSYS simulations (Fig. 14) confirmed this conclusion.

Figure 14 shows the time traces of the pressure at points 1 and 2 near the nozzle exit (see Fig. 2), both for the baseline regime and geometry without aerosol (dashed curve a) and with the aerosol sprayed from the center of the exhaust hole (the solid curves). The following aerosol parameters were used: spray velocity $v = 10$ m/s and flow $j_L = 1.8$ m³/s (liquid volume fraction $f_L = 15\%$), layer thickness $h = 10$ cm, and the droplet diameters $d_{\text{dro}} = 0.25$ mm (curve b) and $d_{\text{dro}} = 0.1$ mm (curve c). Droplet breakup and evaporation were taken into account in the simulation. One can see that, as expected, spikes 3 and 4 are strongly suppressed, whereas

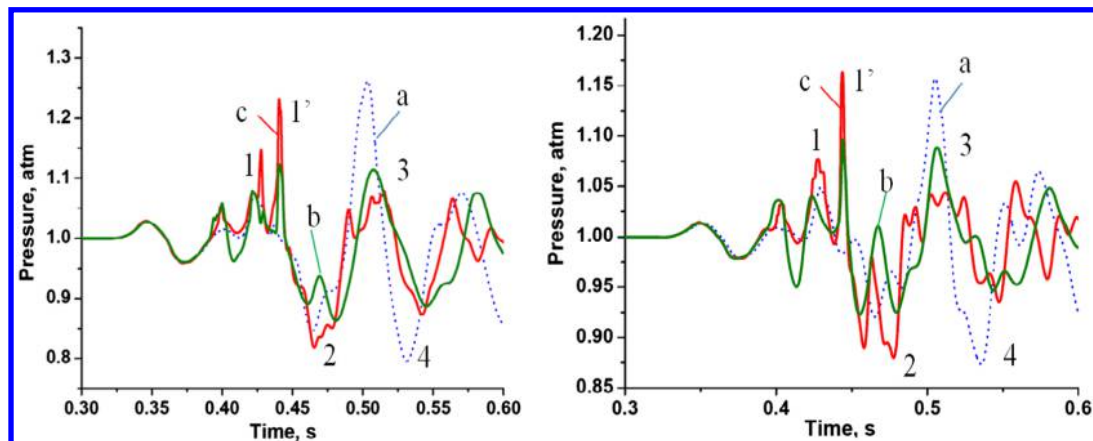


Fig. 14 Pressure at points 1 (right) and 2 (left); no spray (curve a); spray with $d_{\text{dro}} = 0.25$ (curve b) and 0.1 mm (curve c).

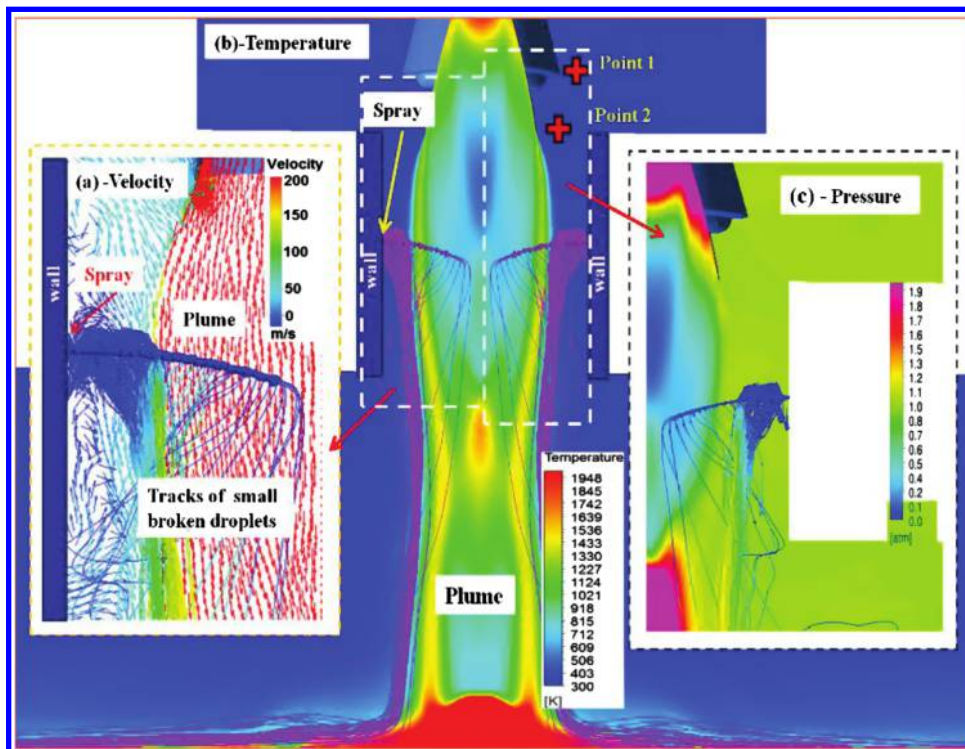


Fig. 15 Velocity (a), temperature (b), and pressure (c) fields at $t = 0.7$ s for a 3 mm droplet spray injected from the center of the exhaust hole.

spikes 1 and 2 are not. Moreover, the amplitude of the inverted spike 2 increases substantially and an extra strong spike (spike 1') appears. This latter spike is caused by the reflection of the first wave, giving rise to spike 1, from the aerosol layer. For the larger initial size of the droplets, they will break up to the minimal size of ~ 0.2 mm during the pulse, as explained in Sec. III.F, and the resulting fine mist will efficiently reflect the wave. A similar effect has been observed in the interaction of shock waves with air–water drop curtains [51]. The magnitudes of the increase in spikes 1 and 2, the formation of spike 1', and the suppression of the other IOP spikes depend on the droplet diameters (Fig. 14).

The droplets of small diameter $d_{\text{drop}} \ll d_{\text{cr,dr}} \approx 0.6$ mm [see Eq. (4)] produce stronger reflection, according to the predictions of Sec. III. The overpressure corresponding to additional spike 1' for

small droplets is $\Delta p_1 = 0.25$ atm. The simulations confirmed the prediction of Sec. III.E: that large droplets are broken up significantly in the regions outside the plume, where the IOP waves propagate. Figure 15 shows the gas velocity [subplot (a)], temperature [subplot (b)], and pressure fields [subplot (c)] at $t = 0.7$ s.

A significant fraction of the droplets has broken up outside the plume area where the gas temperature is $T_g \approx T_L \approx 300$ K, the pressure is $p = 1$ atm, and the gas velocity is $v_g \approx (50\text{--}80)$ m/s. In this region, evaporation of droplets is negligible. Extensive droplet breakup and evaporation are observed inside the plume (see Fig. 15).

The amplitude of IOP spikes 1 and 1' can be successfully reduced by the reflection of the acoustic waves from the aerosol layers created by sprays covering up the area between the nozzle exit and the top of

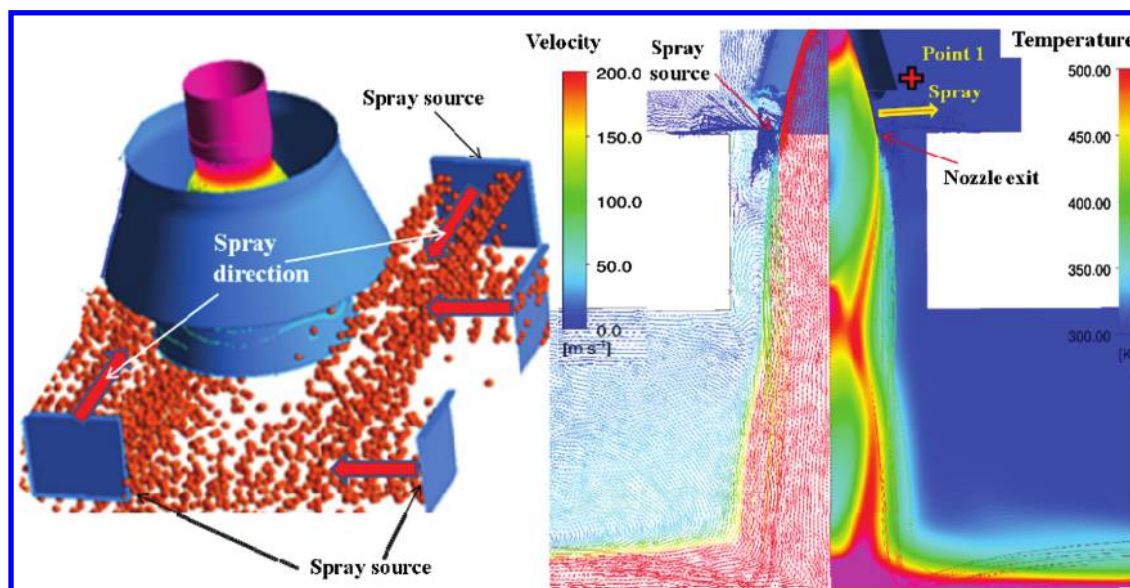


Fig. 16 Spray design for a square exhaust hole (left), and the result of the ANSYS simulation for its radially symmetric version (right).

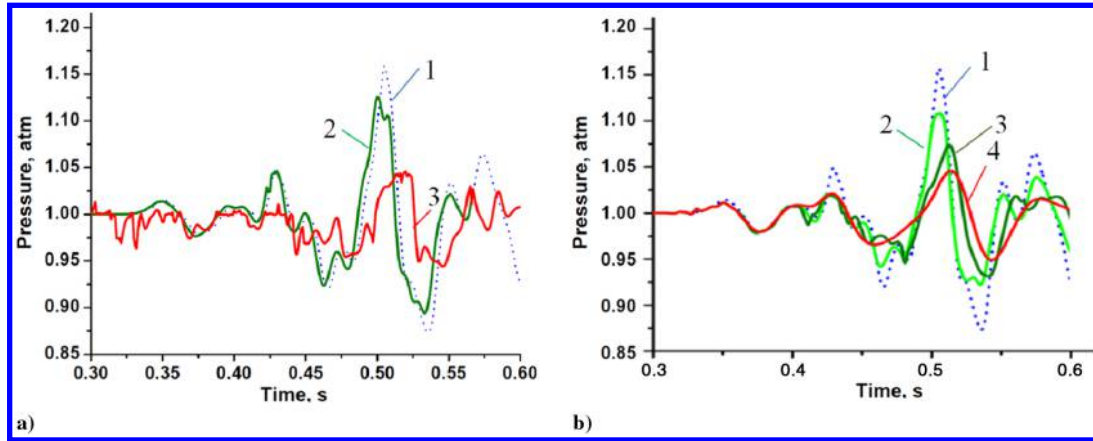


Fig. 17 IOP time traces near the nozzle exit at points 1 for an aerosol spray design presented in Fig. 11 (right).

the exhaust hole. A possible design for a square-shaped exhaust hole is shown in Fig. 16 (left). A set of similar designs for the axisymmetric geometry has been simulated on ANSYS as well. One of these designs is presented in Fig. 16 (right).

Using this spray design reduces all the main IOP spikes, including spike 1 (see Fig. 17, where the results of ANSYS simulations are presented). Dashed lines (lines 1) in Fig. 17 correspond to the regime without aerosol, and the solid lines correspond to the aerosol sprays for width $h = 10$ cm, droplet velocity $v = 10$ m/s, droplet flow $J_{\text{aer}} = 1800$ kg/s ($f_L = 15\%$), and droplet diameters $d_{\text{drop}} = 3$ mm (curve 2) and $d_{\text{drop}} = 0.1$ mm (curve 3) in Fig. 17a; and droplet diameter $d_{\text{drop}} = 0.25$ mm, and droplet flows $J_{\text{aer}} = 720$ kg/s (curve 2, $f_L = 15\%$) and $J_{\text{aer}} = 1800$ kg/s (curve 3) in Fig. 17b.

It is found that mist sprays reflect acoustic waves efficiently. In particular, curve 3 illustrates strong suppression of IOP by the aerosol with $d_{\text{drop}} = 0.1$ mm and mass flow $J_{\text{aer}} = 1800$ kg/s. It is instructive to note that this value of J_{aer} is 4.5 times smaller than the mass flow of the exhaust gas coming from the nozzle. The

suppression effect increases when the mass flow and the width of the aerosol layer increase and the droplet diameter decreases. The suppression effect was found to be the greatest when an extended area above the nozzle was filled by a mist, $d_{\text{drop}} < 0.25$ mm, before the SRB ignition. This was achieved by spraying the mist in the vicinity of the nozzle for 3 s before the ignition started. Curve 4 in Fig. 17 (right) illustrates the degree of IOP suppression in this case.

Droplet breakup and evaporation were taken into account in these simulations. It was found that breakup and evaporation of droplets with $d_{\text{drop}} < 0.25$ mm are negligible outside the plume, even for highest IOP spike 3. Figure 18 shows the gas velocity (a), temperature (b), pressure (c) field, and mass fraction of vapor (d) at $t = 0.7$ s. The droplets are entrained by the shear layer flow of the plume, where they are intensively broken up and evaporate (Fig. 18c and 18d).

For the 5% subscale model, as noted in Sec. III.A, mist corresponds to $d_{\text{drop}} \ll 60$ μm . ANSYS simulations confirmed that, for such small droplets, aerosol suppresses IOP efficiently. Thus, aerosols with initial droplet diameters satisfying the criterion in

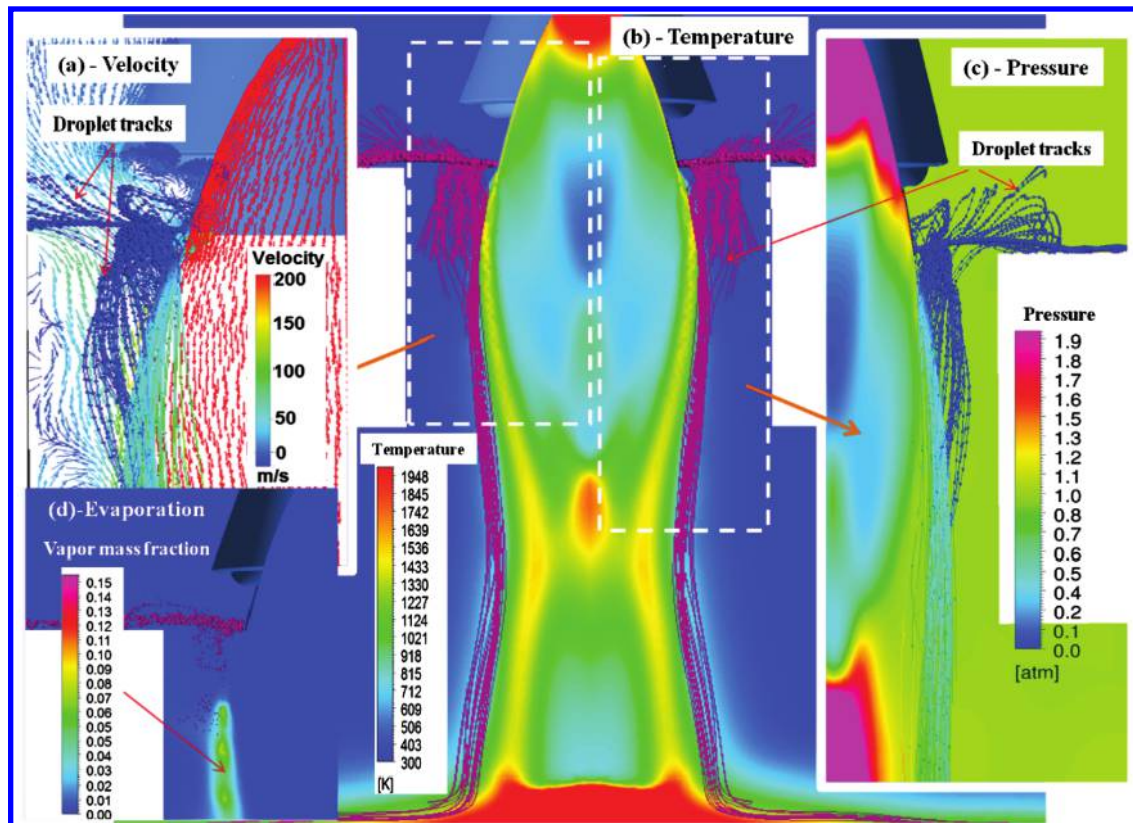


Fig. 18 As in Fig. 15, for sprays injected at the level the nozzle exit.

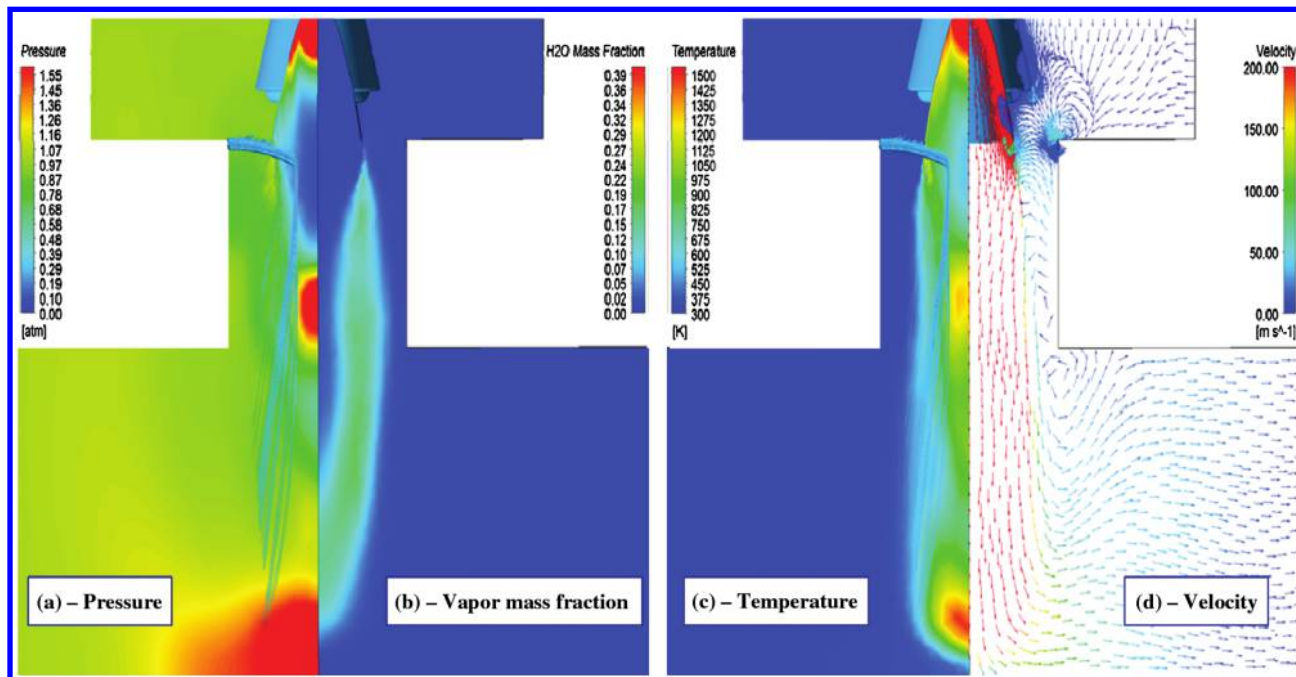


Fig. 19 Spray design of the aerosol streams injected from the periphery toward the plume near the nozzle exit: pressure field, droplets temperature, and droplet traces at the moment $t = 0.434$ s.

Sec. III.A may be used for efficient suppression of IOP pulses in the 5% subscale model.

Another possible design of the spray is shown in Fig. 19, where the aerosol is injected from the periphery toward the plume in the vicinity of the nozzle exit. This spray design reduces all the main IOP spikes (Fig. 20). The dashed line (line 1) in Fig. 20 corresponds to the baseline regime (without aerosol), and the solid lines correspond to the aerosol sprays for width: $h_{\text{aer}} = 10$ cm, droplet velocity $v = 12$ m/s, droplet flow $J_{\text{aer}} = 1800$ kg/s ($f_L = 15\%$), and droplet diameters $d_{\text{drop}} = 0.25$ mm (curve 2) and $d_{\text{drop}} = 0.1$ mm (curve 3).

For this spray design, the aerosol not only covers the exhaust hole from above, and thus suppresses the IOP, but also penetrates into the plume in the region near the nozzle exit, decreasing the gas velocity and temperature in the plume due to the drag and evaporation of the droplets (see Fig. 19, where the results of ANSYS simulations are presented). Figure 19 shows the fields of the pressure (a), the mass fraction of the water vapor (b), the gas temperature (c), and the gas velocity (d). One can see that intensive breakup and evaporation occur inside the plume. It should be noted that the foregoing results hold for particular configuration where the aerosol sprays graze the nozzle lip.

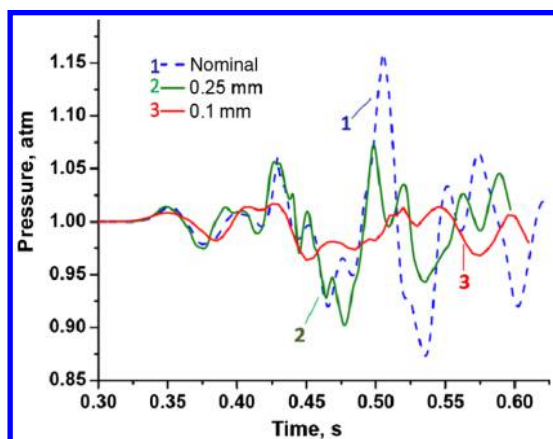


Fig. 20 Pressure at point 1 for the spray injected at the level of nozzle exit for the 5% scale model.

The simulations show that, when a gap exists between the spray and the nozzle lip, the descending wave reflects from the aerosol, enters the gap, and leads to an increase of the overpressure near the nozzle similar to what is observed for the aerosol sprayed from the center of the exhaust hole (Fig. 14).

VI. Conclusions

One of the main conclusions of the present study is that subscale models do not capture the physics of the aerosol-IOP wave interaction in the full-scale rocket. Therefore, subscale data on water suppression should be extrapolated with caution to the full-scale case. It is found that water aerosol layers of high mass loading with small droplets (mists) may effectively reflect the acoustic waves. Such layers can be used to mitigate IOP waves propagating from the exhaust hole to the vehicle. Droplets of sufficiently small size can form as a result of the breakup of large droplets of the water sprays under the action of the IOP pulses for full-scale rockets. On the other hand, the breakup is negligible for the small ($\sim 5\%$) subscale models; therefore, to test mitigation of IOP waves in these models, atomized water sprays (mists with very small droplets) have to be used.

Layers of coarse aerosols with sufficiently large droplets weakly reflect and transmit acoustic waves, even for high mass loading. The transparency of such coarse aerosol layers does not depend on the IOP wavelength but is a function of the droplet size: transparency of the layer increases with the droplet size. Polydisperse aerosols are more transparent than monodisperse aerosols for a given, most likely droplet size. On the other hand, the transmission and reflection coefficients of the mist layers do not depend on the size of the droplets, but rather are complicated functions of the acoustic wave frequency. It is important to note again that, due to droplet breakup, the effective size of the droplets is small in the full-size rocket case and the aerosol is effectively a mist. It is important to note that the superiority of the mists as IOP mitigators compared to coarse aerosols is also confirmed by experimental tests on blast mitigation.

Ideal water sheets (curtains) are found to be equally efficient in mitigating the IOP waves. However, in real spray systems, thin water sheets develop spatial instabilities, resulting in the sheet corrugation and formation of thinning regions, or even sheet breakup, leading to a drastic increase in their transparency to the IOP waves. Aerosols do not develop such instabilities. Another practical advantage of

aerosols is that they can be sprayed over surfaces with complicated geometries, such as the exhaust hole of a heavy lift rocket with several nozzles, where water bags cannot be installed due to the geometrical constraints. In such complicated geometries, it may be impossible to create stable continuous water sheets covering the exhaust hole. As a result, mists are expected to be much more efficient IOP mitigators in practice than water curtains.

Finally, it is worth noting that another way to create a high-density effective medium layer that would reflect the IOP waves away from the launch vehicle is to spray thick foam into the exhaust hole. Foams obtained by adding small amounts of surfactant into water sprayed from the nozzles are expected to behave much in the same way as a fine mist when interacting with long acoustic waves.

References

- [1] Ryan, R. S., Jones, J. H., Guest, S. H., Struck, H. G., Rheinfurth, M. H., and Verderaime, V. S., "Propulsion System Ignition Overpressure for the Space Shuttle," NASA TM-82458, 1981.
- [2] Broadwell, J. E., and Tsu, C. N., "Transient Pressures Caused by Rocket Start and Shutdown in Ducted Launchers," *Journal of Spacecraft and Rockets*, Vol. 4, No. 10, 1967, pp. 1323–1328.
doi:10.2514/3.29079
- [3] Wayte, M. J., and Gruenich, F. A., "Determination of Rocket Ignition Induced Silo Transient Pressures Using an Expansion Tube," *Journal of Spacecraft and Rockets*, Vol. 10, No. 9, 1973, pp. 602–604.
doi:10.2514/3.61933
- [4] Walsh, E. J., and Hart, P. M., "Liftoff Ignition Overpressure-A Correlation," *Journal of Spacecraft and Rockets*, Vol. 19, No. 6, 1982, pp. 550–556.
doi:10.2514/3.62300
- [5] Saito, T., and Nakamura, T., "Numerical Investigation of SRB Ignition Overpressure," *34th AIAA Fluid Dynamics Conference and Exhibit*, AIAA Paper 2004-2342, 2004.
doi:10.2514/6.2004-2342
- [6] Troclet, B., Alestra, S., Terrasse, I., Jeanjean, S., and Srithammavanh, V., "Identification of Overpressure Sources at Launch Vehicle Liftoff Using an Inverse Method," *Journal of Spacecraft and Rockets*, Vol. 44, No. 3, 2007, pp. 597–606.
doi:10.2514/1.21577
- [7] Kiris, C., Housman, J. A., and Kwak, D., "Space/Time Convergence Analysis of a Ignition Overpressure in the Flame Trench," *Computational Fluid Dynamics 2010: Proceedings of the Sixth International Conference on Computational Fluid Dynamics, ICCFD6*, Springer, Berlin, 2010, pp. 645–653.
- [8] Housman, J. A., Barad, M. F., and Kiris, C. C., "Space-Time Accuracy Assessment of CFD Simulations for the Launch Environment," *29th AIAA Applied Aerodynamics Conference*, AIAA Paper 2011-3650, June 2011.
doi:10.2514/6.2011-3650
- [9] Jones, J. H., "Scaling of Ignition Startup Pressure Transients in Rocket Systems as Applied to the Space Shuttle Over-Pressure Phenomenon," *JANNAF 13th Plume Technology Meeting*, CPIA Publ., Houston, TX, April 1982, pp. 371–392.
- [10] Lai, S., and Laspesa, F. S., "Ignition Over-Pressure Measured on STS Lift-Off and Correlation with Subscale Model Tests," *JANNAF 13th Plume Technology Meeting*, CPIA Publ., Houston, TX, 1982, pp. 207–216.
- [11] Dougherty, N. S., Nesman, T. E., and Guest, S. H., "6.4% Scale Model Test Program at NASA/MSFC That Led to Overpressure Reduction of the SSV," *JANNAF 13th Plume Technology Conference*, CPIA Publ., Houston, TX, 1982, pp. 217–224.
- [12] Vu, B. T., Bachchany, N., Peroomianz, O., and Akdag, V., "Multiphase Modeling of Water Injection on Flame Deflector," *21st AIAA Computational Fluid Dynamics Conference*, AIAA Paper 2013-2592, June 2013.
doi:10.2514/6.2013-2592
- [13] Ikawa, H., and Laspesa, F. S., "Space Shuttle Solid Rocket Motor Ignition Overpressure Prediction Methodology," *JANNAF 13th Plume Technology Meeting*, U.S. Dept. of Defense, Chemical Propulsion Information Agency Publ. 357, April 1982, pp. 245–256.
- [14] Ikawa, H., and Laspesa, F. S., "Ignition/Duct Overpressure Induced by Space Shuttle Solid Rocket Motor Ignition," *Journal of Spacecraft and Rockets*, Vol. 22, No. 4, 1985, pp. 481–488.
doi:10.2514/3.25776
- [15] Shapiro, A. H., and Hawthorne, W. R., "The Mechanism and Thermodynamics of Steady One-Dimensional Gas Flow," *Journal of Applied Mechanics*, Vol. 14, No. 4, 1947, pp. A317–A336.
- [16] Woo, J., Jones, J. H., and Guest, S. H., "Study of the Effects of Water Addition on Supersonic Gas Streams," *JANNAF 13th Plume Technology Meeting*, CPIA Publ., Houston, TX, 1982, pp. 225–232.
- [17] Canabal, F., and Frendi, A., "Study of the Ignition Overpressure Suppression Technique by Water Addition," *Journal of Spacecraft and Rockets*, Vol. 43, No. 4, 2006, pp. 853–865.
doi:10.2514/1.14861
- [18] Kailasanath, K., Tatem, P. A., Williams, F. W., and Mawhinney, J., "Blast Mitigation Using Water—A Status Report," Naval Research Lab. Memorandum Rept. 6410-02-8606, 2002.
- [19] Epstein, P. S., *On the Absorption of Sound Waves in Suspensions and Emulsions*, Applied Mechanics: Theodore von Kármán Anniversary Volume, California Inst. of Technology, Pasadena, CA, 1941, pp. 162–188.
- [20] Beranek, L. L., "Acoustical Properties of Homogeneous Isotropic Rigid Tiles and Flexible Blankets," *Journal of the Acoustical Society of America*, Vol. 19, No. 4, 1947, pp. 556–561.
doi:10.1121/1.1916521
- [21] Brekhovskikh, L. M., and Godin, O., *Acoustics of Layered Media I: Plane and Quasi-Plane Waves*, Springer Series on Wave Phenomena, Springer, New York, 1998, pp. 50–57.
- [22] Temkin, S., *Suspension Acoustics*, Cambridge Univ. Press, Cambridge, England, U.K., 2005, pp. 73–81.
- [23] Kandula, M., "Sound Propagation in Saturated Gas-Vapor-Droplet Suspensions with Droplet Evaporation and Nonlinear Relaxation," *Journal of the Acoustical Society of America*, Vol. 131, No. 6, 2012, pp. EL434–EL440.
doi:10.1121/1.4710835
- [24] Kandula, M., "Spectral Attenuation of Sound in Dilute Suspensions with Nonlinear Particle Relaxation," *Journal of the Acoustical Society of America*, Vol. 124, No. 5, 2008, pp. EL284–EL290.
doi:10.1121/1.2987463
- [25] Munson, B. R., Young, D. F., and Okiishi, T. H., *Fundamentals of Fluid Mechanics*, Wiley, New York, 1990, pp. 493–497.
- [26] Wood, A. B., *A Textbook of Sound*, Bell and Sons, London, 1964, pp. 93–97.
- [27] Baranek, L. L., and Work, G. A., "Sound Transmission Through Multiple Structures Containing Flexible Blankets," *Journal of the Acoustical Society of America*, Vol. 21, No. 4, 1949, pp. 419–428.
doi:10.1121/1.1906530
- [28] Babinsky, E., and Sojka, P. E., "Modeling Drop Size Distributions," *Progress in Energy and Combustion Science*, Vol. 28, No. 4, 2002, pp. 303–329.
doi:10.1016/S0360-1285(02)00004-7
- [29] Li, X., "Spatial Instability of Plane Liquid Sheets," *Chemical Engineering Science*, Vol. 48, No. 16, 1993, pp. 2973–2981.
doi:10.1016/0009-2509(93)80042-O
- [30] Eggers, J., "The Subtle Dynamics of Liquid Sheets," *Journal of Fluid Mechanics*, Vol. 672, No. 4, 2011, pp. 1–4.
doi:10.1017/S0022112011000231
- [31] Reitz, R. D., and Diwakar, R., "Structure of High-Pressure Fuel Sprays," SAE Technical Paper 870598, Warrendale, PA, 1987.
doi:10.4271/870598
- [32] Taylor, G. I., *Aerodynamics and the Mechanics of Projectiles and Explosions*, *The Scientific Papers of G. I. Taylor*, edited by Batchelor, G. K., Vol. 3, Cambridge Univ. Press, Cambridge, England, U.K., 1939, pp. 221–250.
- [33] Villermaux, E., and Bossa, B., "Single-Drop Fragmentation Determines Size Distribution of Raindrops," *Nature Physics*, Vol. 5, No. 9, 2009, pp. 697–702.
doi:10.1038/nphys1340
- [34] Pilch, M., and Erdman, C. A., "Use of Breakup Time Data and Velocity History Data to Predict the Maximum Size of Stable Fragments for Acceleration-Induced Breakup of Liquid Drop," *International Journal of Multiphase Flow*, Vol. 13, No. 6, 1987, pp. 741–757.
doi:10.1016/0301-9322(87)90063-2
- [35] Hsiang, L. P., and Faeth, G. M., "Near-Limit Drop Deformation and Secondary Breakup," *International Journal of Multiphase Flow*, Vol. 18, No. 5, 1992, pp. 635–652.
doi:10.1016/0301-9322(92)90036-G
- [36] O'Rourke, P. J., and Amsden, A. A., "The TAB Method for Numerical Calculation of Spray Droplet Breakup," SAE Technical Paper 872089, Warrendale, PA, 1987.
- [37] Liu, B., Mather, D., and Reitz, R. D., "Effect of Drop Drag and Breakup on Fuel Sprays," SAE Technical Paper 930072, Warrendale, PA, 1993.

- [38] Schmehl, R., "Advanced Modelling of Droplet Deformation and Breakup for CFD Analysis of Mixture Preparation," *18th Annual Conference on Liquid Atomization and Spray Systems*, ILASS–Europe, Universidad de Zaragoza, Zaragoza, Spain, Sept. 2002, pp. 1–10.
- [39] Schmehl, R., Maier, G., and Wittig, S., "CFD Analysis of Fuel Atomization, Secondary Droplet Breakup and Spray Dispersion in the Premix Duct of a LPP Combustor," *Proceedings of the Eighth International Conference on Liquid Atomization and Spray Systems*, ILASS Americas, Pasadena, CA, 2000, pp. 918–925.
- [40] Bartz, F. O., Schmehl, R., Koch, R., and Bauer, H. J., "An Extension of Dynamic Droplet Deformation Models to Secondary Atomization," *23rd Annual Conference on Liquid Atomization and Spray Systems*, ILASS–Europe, Brno, Czech Republic, Sept. 2010, pp. 123–136.
- [41] Khare, P., and Yang, V., "Drag Coefficients of Deforming and Fragmenting Liquid Droplets," *25th Annual Conference on Liquid Atomization and Spray Systems*, ILASS Americas, Pittsburgh, PA, May 2013, pp. 1–12.
- [42] Ranz, W. E., and Marshall, W. R., "Evaporation from Drops," *Chemical Engineering Progress*, Vol. 48, No. 3, 1952, pp. 141–146, 173–180.
- [43] *ANSYS Fluid Dynamics Verification Manual*, ANSYS, Pittsburgh, PA, 2011.
- [44] Luchinsky, D., Osipov, V., Hafiychuck, H., Ponizhovskaya, E., Smelyanskiy, V., Dagostino, M., Canabal, F. R., and Mobley, B. L., "Overheating Anomalies during Flight Test due to the Base Bleeding," *Seventh International Conference on Computational Fluid Dynamics*, Paper ICCFD7-3406, Big Island, HI, July 2012, <http://www.iccfd.org/iccfd7/proceedings.html>.
- [45] Dennis, K., Suzen, Y. B., and Mahmud, Z., "Experimental and Computational Investigation of Sonic Reaction Control Jets into Supersonic Cross-Flows," *37th AIAA Fluid Dynamics Conference and Exhibit*, AIAA Paper 2007-3860, June 2007.
- [46] Chougule, N. K., Parishwad, G. V., Gore, P. R., Pagnis, S., and Sapali, S. N., "CFD Analysis of Multi-Jet Air Impingement on Flat Plate," *Proceedings of the World Congress on Engineering 2011*, Vol. III, London, July 2011, pp. 2431–2435.
- [47] Frank, T. H., Lifante, C., Prasser, H.-M., and Menter, F., "Simulation of Turbulent, and Thermal Mixing in T-Junctions Using URANS, and Scale-Resolving Turbulence Models in ANSYS CFX," *Journal of Nuclear Engineering, and Design (NED)*, Vol. 240, No. 9, 2010, pp. 2313–2328.
doi:10.1016/j.nucengdes.2009.11.008
- [48] Kuntz, M., "Automotive Simulation World Progress," *Validation and Verification of ANSYS Internal Combustion Engine Software*, ANSYS, Pittsburgh, PA, Oct. 2012, pp. 1–66.
- [49] Frank, T. H., Kumzerova, E., and Esch, T. H., "Validation of Lagrangian Spray Formation for Use in Internal Combustion Engines," *5th Joint FZR and ANSYS Workshop Multiphase Flows: Simulation, Experiment and Application*, Dresden, Germany, April 2007, pp. 1–27, http://www.drthfrank.de/publications/2007/Frank_Kumzerova_Esch_SpraySimulations_Dresden2007.pdf.
- [50] Frank, T. H., "Validation of Multiphase Flow Modeling in ANSYS CFD" *SIAMUF — Swedish Industrial Association for Multiphase Flows, Multiphase Flows Meeting, Short Course and Seminar*, Säröhus, Säröhusvägen, Särö/Gotenburg, Norway, Oct. 2009, pp. 1–73, http://www.tfd.chalmers.se/siamuff/ian_hamill.pdf.
- [51] Buzukov, A. A., "Decreasing the Parameters of an Air Shock Wave Using an Air-Water Curtain," *Combustion, Explosion, and Shock Waves*, Vol. 36, No. 3, 2000, pp. 395–404.
doi:10.1007/BF02699393

R. Cummings
Associate Editor